Diurnal Variation of the Planetary Boundary Layer in a Mesoscale Model

I. ORLANSKI, B. B. ROSS AND L. J. POLINSKY

Geophysical Fluid Dynamics Laboratory/NOAA, Princeton University, Princeton, N.J. 08540

(Manuscript received 27 August 1973, in revised form 20 December 1973)

ABSTRACT

A two-dimensional mesoscale atmospheric model is presented and used to study unsteady dynamic processes occurring in the planetary boundary layer (PBL) driven by diurnal heating at the ground. The model reproduces turbulent fluxes of heat and momentum both by explicitly modeling resolvable eddies and by employing a single parameterization at all levels of the model to represent vertical fluxes caused by subgrid-scale eddies. The unsteady behavior of horizontally-averaged profiles of temperature and velocity respond quite realistically to the diurnally-varying heat flux at the ground, particularly with regard to the time variation of lapse rates and the occurrence times of maximum and minimum temperatures at various levels in the lower boundary layer. The spatial variation of predicted atmospheric quantities shows a great deal of resolved eddy activity during the day with a significant remnant persisting through the night at higher levels of the PBL. These eddies account for the predominant means of vertical heat and momentum transfer away from the surfaces with the model realistically reproducing the unsteady behavior of heat fluxes in the PBL. Temporal variation of vertical heat and momentum profiles shows boundary layer activity to be confined to a few hundred meters at night while extending up to a kilometer during the day. A weak heat flux source at the ground with an amplitude of 10% of the maximum daytime heating produced a nocturnal heat island some 60 m high with a maximum city-country temperature contrast of $\sim$1C.

1. Introduction

Meteorologists have historically tended to study atmospheric dynamics from two points of view which are characterized by greatly differing space and time scales. In trying to explain the detailed behavior of the immediate surface environment in which Man lives, they have developed the science of micrometeorology which deals with atmospheric dynamics having space scales of several meters and time scales on the order of a minute. Similarly, in order to predict the evolution of weather patterns in the atmosphere, meteorologists have devoted much attention to the behavior of large-scale dynamics having space scales greater than 1000 km and time scales of the order of a week.

Yet although macro- and microscale meteorology encompasses many atmospheric processes, there is still a large number of important phenomena occurring in the atmosphere whose spatial and temporal scales are intermediate between these two categories. The slowness with which our understanding of these intermediate scales has developed has been caused, not by their lack of importance, but rather by the difficulty involved in obtaining useful observational data concerning them. However, the recent surge of interest in the urban environment and in severe storm weather conditions has reversed this trend and seems to be leading to a more rapid advancement of our understanding of these important meteorological processes.

The wide range of atmospheric phenomena with scales between the macro- and microscales necessitates the further division of processes according to time and space scales. A logical grouping which is commonly accepted and which will be used here is to define "intermediate-scale" and "mesoscale" categories. Intermediate-scale dynamics, with scales of the order of 1000 km and several days, are characterized as being direct by-products of the large-scale motion. On the other hand, mesoscale phenomena are characterized by time scales between several hours and one day and space scales between ten and several hundred kilometers, and although they are affected by the prevailing large-scale weather systems, their dynamics are largely controlled by local energy sources.

Many examples of mesoscale phenomena exist in the atmosphere; for example, there are local severe storms such as thunderstorms and storms producing tornadoes, cloud clusters, orographic phenomena such as mountain lee waves, land-sea breezes, the low-level nocturnal jet, and man-made atmospheric effects such as the urban heat island. It is clear from this list that mesoscale processes will be influenced by large-scale dynamics in creating and changing the local prevailing weather conditions as well as by microscale phenomena such as turbulent mixing which account for eddy transfer processes and dissipation at the high-wavenumber end of the energy spectrum. Conversely, the collective effect of mesoscale processes often may be strong enough to alter large-scale weather systems, not only by means of

direct, local interaction with the macroscale dynamics, but also through distant interaction of the large-scale dynamics with gravity waves generated by the meso-scale phenomena.

In the present paper, we will present and discuss several basic solutions produced by a two-dimensional finite-difference flow model which is capable of simulating a number of different mesoscale phenomena. Our primary interest in this initial study will be directed toward the fundamental mesoscale problem of the un-steady response of the planetary boundary layer (PBL) to the diurnal variation of atmospheric heating at the surface. In the same solutions, we will also investigate the formation of a heat island dome above a weak localized surface heat source such as might be produced by a city (but without including complicating factors such as pollution chemistry and increased surface roughness due to buildings).

In Sections 2 and 3, the mathematical formulation of the mesoscale model is presented, together with the specific physical parameters and boundary conditions which distinguish the two solutions to be discussed. The computed solutions for the PBL layer are then described and discussed in Sections 4, 5 and 6 in terms of the behavior of horizontally-averaged quantities, spatially-varying quantities, and boundary layer fluxes near the ground. Relevant observational data are also presented in these later sections when comparison with the computed solutions is possible.

2. Mathematical model

The mesoscale model presented here uses the "deep anelastic" equations as formulated by Ogura and Phillips (1962). Since the horizontal scale of interest is on the order of 100 km or less, we assume that the Coriolis parameter f is constant. Although mesoscale dynamics are characteristically three-dimensional, as a first attempt to understand these processes and to test our model, we simplify the model by assuming that the predicted quantities do not depend on one of the horizontal Cartesian coordinates (namely y). However, in order to incorporate rotational effects, we need to retain the velocity component in the y direction. Because the mesoscale dynamics are assumed to be partially driven by a large-scale geostrophic flow, a horizontal temperature gradient consistent with the thermal wind relation is included in the y direction. We also assume that the atmosphere is dry.

The primitive equations are

$$\frac{\partial V}{\partial t}+V\cdot\nabla V+f k\times V= -c_p\theta\nabla\pi-g k+\frac{1}{\rho_0}\nabla\cdot\tau, \quad (2.1)$$

$$\nabla\cdot\rho_0 V=0, \quad (2.2)$$

$$\frac{\partial\theta}{\partial t}+V\cdot\nabla\theta=\nabla\cdot F+\Re, \quad (2.3)$$

where V is the three-dimensional velocity vector with components u, v, w in the x, y, z directions respectively; ρ_0 is the mean density (a known function of z); θ the potential temperature defined as $\theta\equiv T(P/P_s)^{-R/c_p}$; $\pi\equiv(P/P_s)^{R/c_p}$; $\Re$ represents the radiation term; and τ and F represent the turbulent momentum stress tensor and turbulent heat flux vector respectively. Using the previous assumptions, we can simplify all these equations in the following manner using streamfunction ψ and vorticity ζ for motion in the x-z plane:

$$\frac{\partial\zeta}{\partial t}-J(\psi,\alpha\zeta)-f\frac{\partial v}{\partial z}=\frac{g}{\theta_s}\frac{\partial\theta}{\partial x}+\nabla\cdot\nu_e\nabla\zeta, \quad (2.4)$$

$$\frac{\partial v}{\partial t}-\alpha J(\psi,v)+f\left(\frac{\alpha\partial\psi}{\partial z}-\bar U_g\right)=\nabla\cdot\nu_e\nabla v, \quad (2.5)$$

$$\zeta=\frac{\partial}{\partial x}\left(\alpha_0\frac{\partial\psi}{\partial x}\right)+\frac{\partial}{\partial z}\left(\alpha_0\frac{\partial\psi}{\partial z}\right), \quad (2.6)$$

$$\frac{\partial\theta}{\partial t}+v\frac{\partial\bar\theta_g}{\partial y}-\alpha_0 J(\psi,\theta)=\nabla\cdot K_e\nabla\theta+\Re, \quad (2.7)$$

where

$$\alpha_0-1/\rho_0=\alpha_s\left(1-\frac{g}{c_p\theta_s}z\right)^{-[(c_p/c_v)-1]},$$

and ψ is defined such that $\partial\psi/\partial z=u/\alpha_0$ and $\partial\psi/\partial x=-w/\alpha_0$. Notice also that the advective terms have been manipulated such that they are in Jacobian form for the sake of numerical considerations. The turbulent momentum and heat fluxes have been parameterized using eddy diffusivity coefficients ν_e and K_e which will be described below. The term $f[\alpha(\partial\psi/\partial z)-\bar U_g]$ in (2.5) represents the ageostrophic component of the Coriolis force and $v\partial\theta/\partial y$ of (2.7) represents the advection of temperature due to the large-scale temperature field. Accordingly, it is clear that $\partial\theta_g/\partial y$ is related to U_g by the thermal wind relation $(\partial\theta_g/\partial y)=\theta_g(f/g)(\partial U_g/\partial z)$.

In formulating the turbulent flux parameterization to be used in this stratified atmospheric model, it is important for us to recognize the great diversity of processes which are capable of producing turbulence in stratified flows (for example, Kelvin-Helmholtz instability, penetrative convection, gravity wave interaction, etc.). It seems unlikely that these many different processes will exhibit a similar dependence upon the local velocity field as is implied by the explicit velocity deformation dependence prescribed in a number of previous subgrid turbulence parameterizations applied to stratified flows (Lilly, 1962; Estoque, 1963; Deardorff, 1969). Because of the absence of an unambiguous correlation between velocity deformation and these turbulence-generation mechanisms taken as a whole, we have chosen here to take a different approach from these earlier eddy viscosity formulations.

Thus in characterizing all of the different turbulence generation processes, we will assume that turbulence in stratified fluids is ultimately produced by only two mechanisms: (i) convective instability if the mean stratification is unstable and (ii) wave breaking if the mean stratification is stable. We will thus take the point of view [a more complete description of this approach as well as a review of other eddy viscosity formulations is given by Orlanski and Ross (1973)] that subgrid turbulent fluxes will only occur at those locations in the model where local gravitational instability is produced by flow processes which are resolved by the model. Eddy viscosity and diffusivity will thus only depend upon local statically-unstable gradients of potential temperature in our model.

It is important to emphasize that, although this eddy viscosity form does not explicitly involve deformation, the formulation will still model turbulence generation caused by shear as well as other instabilities in stratified flow to the extent that the development of these instabilities is resolved by the numerical model. The manner in which this representation occurs is exemplified by the case of Kelvin-Helmholtz instability. In regions of shear with stable stratification, unstable waves will develop naturally in the numerical computation where conditions are favorable for Kelvin-Helmholtz instability, typically in regions of sufficiently low Richardson number. If favorable conditions persist for a sufficient time, these waves will grow to the point where overturning occurs at certain locations in the developing wave field. Eddy viscosity will then be activated in these gravitationally unstable regions, thereby producing effective subgrid eddy fluxes and quenching the shear instability. (The activation of this eddy viscosity formulation in regions which are stable in the mean will be demonstrated in Section 6 in which nighttime eddy viscosity at 400 m height is shown to be nearly five times its background value even though the mean temperature stratification in this region is statically stable.)

The specific details of the dependence of eddy viscosity upon the unstable potential temperature gradient do not appear to be crucial in the model. This will be demonstrated later by reference to Table 2 which shows the effective eddy diffusivity generated in the solution away from the ground due to resolved eddies to be several orders of magnitude larger than the local parameterized eddy values during the daytime when turbulent activity is strongest. As regards the parameterization of subgrid-scale quasi-steady convection in the model, two different approaches will be considered here in relating vertical heat flux to local temperature gradients. Priestley (1954) used dimensional analysis with the assumption that heat flux is independent of molecular diffusion coefficients in atmospheric convection to infer that heat flux depends on $(\partial\theta/\partial z)^{\frac{3}{2}}$ and thus that eddy diffusivity K_e depends on $(-\partial\theta/\partial z)^{\frac{1}{2}}$. On the other hand, laboratory experiment (Globe and Dropkin, 1959) and theoretical analysis

(Kraichnan, 1962) concerning free convection without wind at high Rayleigh numbers show that the non-dimensional heat flux in the form of Nusselt number is proportional to the one-third power of the Rayleigh number Ra [defined as $g\Delta\theta\Delta z^3/(\theta\kappa\nu)$, where κ and ν are molecular diffusivity and viscosity] and thus implying that K_e is proportional to $(-\partial\theta/\partial z)^{\frac{1}{3}}$ for constant Prandtl number. Ingersoll (1966) has found experimentally that this latter result (as well as the proportionality of nondimensional momentum flux to $Ra^{\frac{1}{3}}$) continues to be valid in flows with weak velocity shear.

Neither the $\frac{1}{2}$- nor the $\frac{1}{3}$-power formulation is totally justified for use in this present atmospheric model. Priestley's formulation, which depends upon $(-\partial\theta/\partial z)^{\frac{1}{2}}$, was derived for very high Rayleigh numbers and strong convection and thus will not be appropriate for parameterizing gravitational instability in waves or even convection in the surface layer when convective instability is weak as in the early daytime hours. The second formulation, depending on $(-\partial\theta/\partial z)^{\frac{1}{3}}$, depends on molecular values and is thus not suitable for atmospheric conditions.

We have chosen here to use the $\frac{1}{3}$-power dependence of eddy viscosity on unstable potential temperature gradient because we feel that this weaker dependence on unstable stratification more accurately represents the moderate levels of convection which occur on the subgrid scales. In our model, we will assume that the atmosphere maintains a weak level of turbulence in stably-stratified conditions, with this turbulence level represented by a constant background eddy viscosity and diffusivity in the formulation. (These diffusion coefficients are also felt to be necessary in order to reduce numerical noise for strongly stable conditions, in which case the variable eddy viscosity is not activated). Then in order to facilitate the formulation of eddy viscosity in unstably-stratified conditions, we will define a local Rayleigh number which is based on these background eddy diffusion coefficients rather than on molecular values as were used in the classical Rayleigh number definition employed by Kraichnan (1962). Using this new Rayleigh number raised to the $\frac{1}{3}$ power, we then obtain an eddy diffusivity of the form

$$K_e = \begin{cases} K_0\left[1+C\left(-\dfrac{g\Delta\theta(\Delta z)^3}{\theta K_0\nu_0}\right)^{\frac{1}{3}}\right], & \text{if } \Delta\theta < 0 \\ K_0, & \text{if } \Delta\theta \geqslant 0 \end{cases} \qquad (2.8)$$

where K_0 and ν_0 are the constant background values of eddy diffusivity and viscosity, and Δz and $\Delta\theta$ are local values of the vertical grid size and potential temperature difference across the grid box, respectively. The eddy viscosity ν_e will be proportional to K_e with the assumed proportionality constant to be discussed in the next section.

Although we realize that radiation plays an important role in the energy balance of the lower atmosphere at

certain times of the day, we will parameterize the radiation effect in a very simple form as

$$\Re = R\frac{\partial^2\theta}{\partial z^2}, \qquad (2.9)$$

where the values of the constant R will be given in Table 1 and discussed in Section 3.

In order to avoid the complexities of open boundary conditions, we will use cyclic boundary conditions at the inflow and outflow boundaries, $x=0$ and $x=L$, respectively. The non-slip boundary conditions $u=v=w=0$ are used at $z=0$. The two conditions $w=v=0$ can be satisfied by requiring that $\psi=v=0$ at $z=0$. However, since we do not use the primitive equations, we must specify a boundary condition for vorticity in order to constrain u to be zero at the boundary. Two different methods for doing this will be described in the next section.

One of the most important driving forces for this mesoscale model is the heat flux from the ground. Since we will not compute an energy heat balance at the soil-atmosphere interface, we prescribe the surface heat flux into the atmosphere to be a known function of time and space. The different forms of this heat flux will be described in the next section.

Since the top of the model ($h=10$–20 km) is remote from the dynamically active layer of the model (the first few thousand meters), we do not feel that the formulation of this boundary condition will be crucial to the overall solution. We have assumed the following boundary conditions for this top boundary: $\zeta=\partial v/\partial z$ $=0$; ψ and $\partial\theta/\partial z$ fixed at their initial values. These conditions are imposed in order to reduce the reflection of waves from this boundary.

3. Formulation of the numerical model

As we mentioned in the previous section, one of the primary driving forces in the model is the heating of the atmosphere from the ground. Therefore, it seems reasonable to increase the model resolution near the ground in order to better resolve the small-scale behavior caused by this heating. Accordingly, we will transform the vertical physical coordinate z into a coordinate Z given by the relation $Z=Z(z)$ (Table 1), different forms of which will be prescribed later in this section. Eqs. (2.4)–(2.7) may then be written as

$$\frac{\partial\zeta}{\partial t}=GJ(\psi,\alpha_0\zeta)+gG\frac{\partial v}{\partial Z}-\frac{g}{\theta_s}\frac{\partial\theta}{\partial x}$$

$$+\frac{\partial}{\partial x}\left(\nu_e\frac{\partial\zeta}{\partial x}\right)+G\frac{\partial}{\partial Z}\left(G\nu_e\frac{\partial\zeta}{\partial Z}\right), \quad (3.1)$$

$$\frac{\partial v}{\partial t}=\alpha_0GJ(\psi,v)+\alpha_0 f\left[G\frac{\partial\psi}{\partial Z}-U_g\right]$$

$$+\frac{\partial}{\partial x}\left(\nu_e\frac{\partial v}{\partial x}\right)+G\frac{\partial}{\partial Z}\left(G\nu_e\frac{\partial v}{\partial Z}\right), \quad (3.2)$$

$$\zeta=\alpha_0\frac{\partial^2\psi}{\partial x^2}+G\frac{\partial}{\partial Z}\left(\alpha_0 G\frac{\partial\psi}{\partial Z}\right), \quad (3.3)$$

$$\frac{\partial\theta}{\partial t}=\alpha_0GJ(\psi,\theta)+\left(\frac{f\theta_s}{g}G\frac{dU_g}{dZ}\right)v$$

$$+\frac{\partial}{\partial x}\left(K_e\frac{\partial\theta}{\partial x}\right)+G\frac{\partial}{\partial Z}\left(GK_e\frac{\partial\theta}{\partial Z}\right)+GR\frac{\partial^2\theta}{\partial Z^2}, \quad (3.4)$$
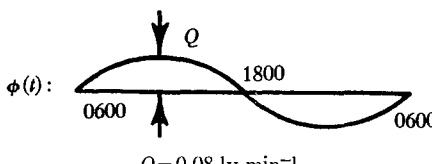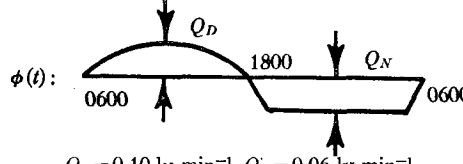
where $G=dZ/dz$ and the horizontal coordinate x is unchanged. These equations are approximated by a finite-difference form analogous to that used by Orlanski and Ross (1973). In this formulation a centered space and time difference approximation is used to represent the space and time derivatives. The Jacobians of these equations are treated by the methods of Arakawa (1966) and Lilly (1965) to minimize non-linear instability. The leap-frog method is used for time differencing but with the diffusive terms lagged one time step. The solution is time-smoothed every 30 time steps to minimize mode splitting which is associated with the leap-frog method. The solution of Poisson's equation (3.3) is obtained by a standard Fourier decomposition algorithm in an analogous manner to that described by Orlanski and Ross.

In developing the present model (which hereafter we shall refer to as Experiment II), we have performed a series of experiments in which we have altered the model boundary conditions, the numerical resolution, and the initial conditions. For the sake of comparison in the discussion which follows, we will present the results from these previous solutions, which are referred to as Experiments Ia and Ib. A summary of the major differences between these experiments is presented in Table 1.

a. Domain size and model resolution

In order to resolve the dynamic activity of the lower 5000 m in Experiment I (including Ia and Ib), we felt that logarithmic stretching was appropriate and also that it had the additional advantage of allowing us to extend the upper boundary to a height $h[=20$ km$]$ far above the dynamically active layer at the cost of a few additional grid levels. The specific form of the coordinate transformation $Z(z)$ can be seen in Table 1. With 70 levels in Experiment I we obtain a resolution of $\Delta z=3$ m at the ground and $\Delta z=1700$ m in the levels near the top of the model. The horizontal domain spans a distance of 60 km with a grid resolution of $\Delta x=1.87$ km (32 grid points).

TABLE 1. Summary of differences between Experiments Ia and Ib and Experiment II with regard to vertical coordinate transformation, numerical and physical constants, and initial and boundary conditions. See text for details.

	Experiment Ia	Experiment Ib	Experiment II
$Z(z)$	$Z = \dfrac{\ln\left(\dfrac{z+30.5}{30.5}\right)}{\ln\dfrac{h+30.5}{30.5}}$		$Z = \dfrac{z}{1600} + \dfrac{1}{17.9}\ln\left(\dfrac{z+15}{15}\right)$
L h Δx	60,000 m 20,000 1874		30,000 m 10,160 937
K_0 ν_e/K_e C	0.0093 m² sec⁻¹ 1.00 0.10		0.0900 m² sec⁻¹ 0.70 0.30
R	0.117 m² sec⁻¹	0.351 m² sec⁻¹	0.100 m² sec⁻¹
$H(x,t)$	$H = \phi(t)\left\{1+0.15\exp\left[-\left(\dfrac{x-30000}{7500}\right)^2\right]\right\}$ $Q = 0.08$ ly min⁻¹		$H = \phi(t)+0.10\,Q_D\exp\left[-\left(\dfrac{x-15000}{3750}\right)^2\right]$ $Q_D = 0.10$ ly min⁻¹, $Q_N = 0.06$ ly min⁻¹
ζ_s	$\zeta_s = \dfrac{2\alpha_{0s}}{(\Delta z)^2}\psi_{z=\Delta z}$		$\zeta_s = \left(\dfrac{u^2}{u^2+v^2}\right)^{\frac{1}{2}}_{z=\Delta z}\dfrac{u^*}{kz_0}\phi_m\left(\dfrac{z_0}{L_m}\right)$
$U_0(z)$	$U_0 = \begin{cases} 24.6\dfrac{z}{7000}\left(2-\dfrac{z}{7000}\right),\ z<7000\text{ m} \\ 24.6,\ z>7000\text{ m} \end{cases}$		$U_0 = 15.7\,\tanh\left(\dfrac{z}{1500}\right)$
$U_g(z)$	$U_g = U_0$		$U_g = 4+11\,\tanh\left(\dfrac{z}{1500}\right)$
	Solution time Exp. Ia: from initial conditions at 0600 of Day 1 to 0955 of Day 2. Exp. Ib: started from solution of Exp. Ia at 1800 Day 1; stopped at 1950 of Day 2.		Solution time From initial conditions at 0600 of Day 1 to 0100 of Day 3.

Our experience with Experiment I has shown that the coarser resolution in the upper layers of the model produced a significant distortion of the gravity waves propagating upward from the active lower layers. To more effectively resolve this wave propagation, we decided to adopt a log-linear coordinate transformation (see Table 1) for Experiment II. In this case, using 80 levels, we have a similar resolution in the lower boundary layer with $\Delta z = 3.7$ m at the surface, but a nearly constant grid resolution of $\Delta z \approx 175$ m from $z = 4000$ m to the top of the domain ($h = 10,160$ m). Note here that we have lowered the top boundary location, but have found that this does not affect the solution significantly in the boundary layer. Also, we have increased the horizontal resolution to $\Delta x = 937$ m which gives a span L of 30 km using the same number of grid points as before.

b. Lower boundary conditions

In modeling the heat flux into the atmosphere from the ground, we chose a sinusoidal time dependence for Experiment I with a period of one day and no net daily heat flux. For the spatial distribution we assumed a Gaussian distribution centered at $x = L/2$ with an e-folding factor of 7.5 km. This arbitrary spatial function was selected to simulate a concentrated surface heat source such as the heating produced by a city. The ratio between the maximum heating at the center of the model and the background heating at both sides is approximately 1.15, with the maximum background heating equal to 0.08 ly min⁻¹.

The boundary condition for surface vorticity ζ_s at $z = 0$ in Experiment I is

$$\zeta_s = \frac{2\alpha_{0s}}{(\Delta z_s)^2}\psi\bigg|_{(z=\Delta z_s)}, \qquad (3.5)$$
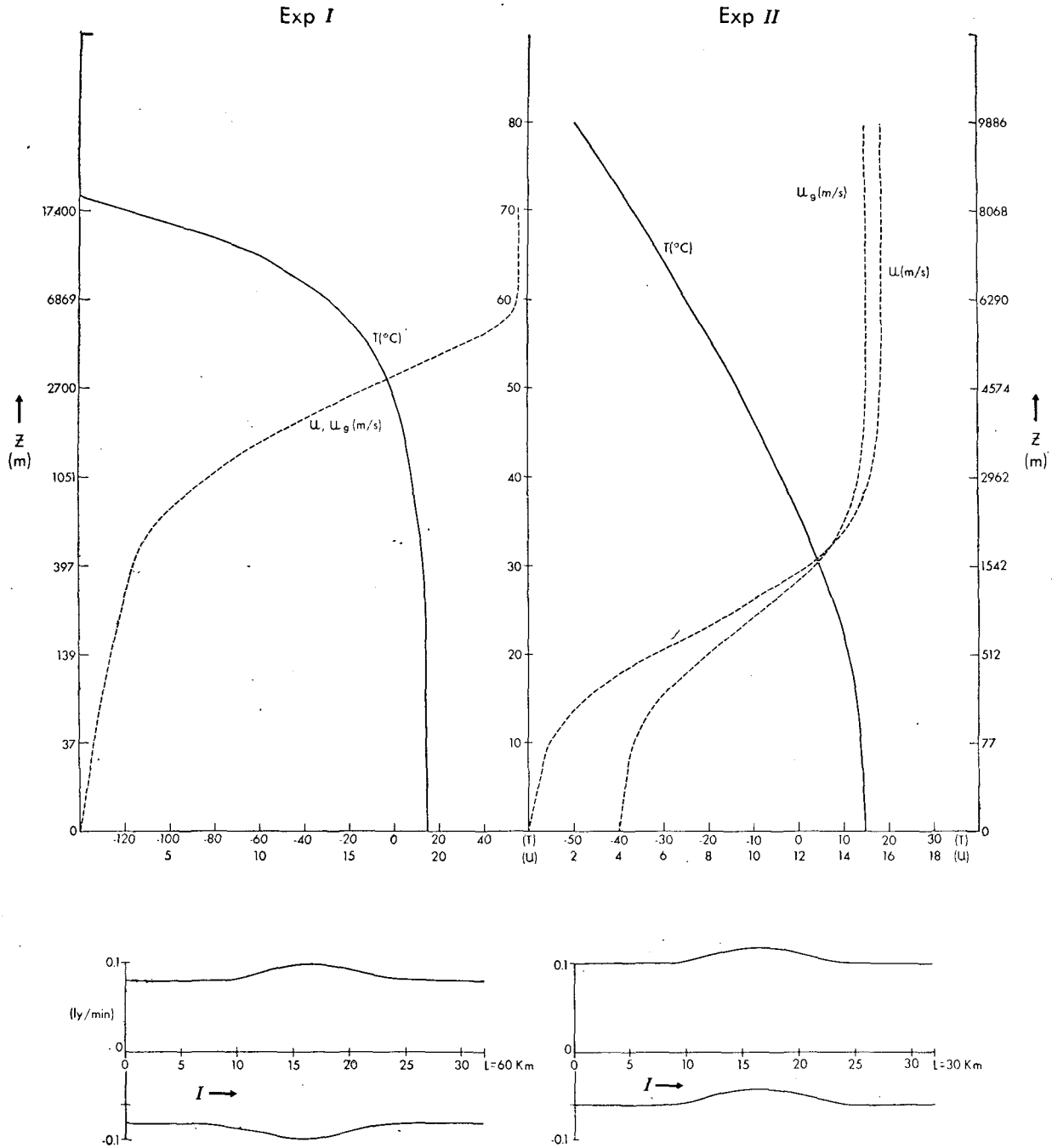
FIG. 1. Profiles of initial temperature $T(^\circ C)$, initial x component of wind u (m sec^{-1}), and constant geostrophic wind u_g (m sec^{-1}) for Experiments I and II plotted against the vertical grid number J (center vertical scale) with corresponding values of height z (m) for each numerical experiment (shown on the left and right vertical scales). The assumed heat flux distributions (ly min^{-1}) at times of maximum daytime heating and maximum nighttime cooling for each experiment are shown in the bottom of the figure and are plotted against horizontal grid number I.

where Δz_s is the vertical grid size at the ground. This condition implies, in finite-difference form, the vanishing of the extrapolated value of u and w at $z=0$.

The heat flux and the vorticity formulation presented above were shown to be too crude to provide a realistic simulation of the boundary layer. In the first place, it

is known that the net radiative cooling at the lower boundary of the atmosphere is fairly constant between sunset and sunrise, thus making our previous boundary heating condition for Experiment I unrealistic during this period. We thus have replaced this boundary condition in Experiment II with an empirical formula

in which the heating is sinusoidal in time during the day but the cooling is constant at night (see Table 1). Another defect of the previous boundary condition was that the Gaussian heating contribution was oscillatory in time; accordingly, this caused maximum heating during the day and maximum cooling at night (a result which is in conflict with usual observations of urban heat island phenomena). In Experiment II we thus have imposed a Gaussian distribution of heat for the whole diurnal cycle which is invariant in time and therefore represents a constant heat source. The ratio of the maximum amplitude of the Gaussian heating to the maximum daytime amplitude of the background heating is 0.10 in Experiment II. The ratio of the amplitudes of maximum daytime heating to the constant nighttime cooling is 1.67, thus producing a nearly vanishing net heat flux over a diurnal cycle (see Fig. 1).

Concerning the vorticity boundary condition of the previous experiment, the assumed validity of a linear extrapolation of velocity over the first 3 m above the ground is in conflict with the known logarithmic behavior in this region, and, in fact, the solution from Experiment 1 shows u to not approach zero at the bottom boundary. We have thus sought to improve this in Experiment II by directly predicting the vorticity using the Monin-Obukhov universal function ϕ_m at the bottom of the model ($z=0$) which is located at the roughness height z_0 (which was here chosen to be constant and equal to 0.1 m). The relation for the surface vorticity is thus given by

$$\zeta_s = \left[\frac{u}{(u^2+v^2)^{\frac{1}{2}}} \right]_{z=\Delta z} \frac{u^*}{kz_0} \phi_m(z_0/L_m), \qquad (3.6)$$

where u^* is the friction velocity and L_m the Monin-Obukhov length, both of which are assumed to be constant over the first few meters of the atmosphere and are thus calculated at the first grid point above the ground. In this equation, we have used the functional form of ϕ_m as obtained from the observations of Businger et al. (1971); ϕ_m will be formally defined in Section 6. Note that the vorticity is corrected to include only the x contribution of the shear since the y contribution is explicitly computed.

c. Physical constants and initial conditions

One of the unique aspects of the present model is that we are able to simulate turbulent transfer processes over different layers using a single parameterization which is applied over the entire depth of the modeled atmosphere as given in Eq. (2.8). This is in contrast to the approaches of other investigators (Estoque, 1963; Pandolfo, 1971) who used different parameterizations for different regions above the surface. The constants used in this parameterization for Experiments I and II are shown in Table 1. In particular, we should point out that the eddy diffusion coefficients in Experiment II

are approximately an order of magnitude larger than in Experiment I.

The constants R used in the radiation parameterization (2.9) for the numerical experiments are also shown in Table 1. Note, in particular, that parallel calculations have been run in Experiment I (distinguished as Experiments Ia and Ib) in which only the radiation constant R has been varied. As we shall see in Section 6, radiation effects in the model are confined to regions of strong temperature gradients in the lowest 10 m of the atmosphere during the day but extend up to a height of 50 m or more at night. A comparison between Experiments Ia and Ib will only show major differences between the solutions near the ground at night in those regions in which radiation transports a large part of the heat flux to the ground.

The initial conditions for Experiments I and II are summarized in Fig. 1. Both experiments use the same initial conditions for temperature prescribed such that potential temperature has a linear profile which increases with height at a rate of 4C $(100 \text{ m})^{-1}$. In Experiment I we have assumed a parabolic profile for u with the velocity going to a constant value of approximately 25 m sec^{-1} above 7000 m (see Table 1). This initial u profile was exactly the same as the geostrophic wind profile $U_g(z)$ used in Eqs. (3.2) and (3.4), implying that the geostrophic flow already satisfies the non-slip conditions at the ground and will not produce an Ekman balance in the lower layers of the atmosphere.

In Experiment II, on the other hand, the geostrophic wind was assumed to take the form of a hyperbolic tangent with a velocity going to 15 m sec^{-1} at approximately 3000 m but with the wind going to a value of 4 m sec^{-1} at the ground. The initial wind profile $U(z)$ was assumed to take a similar form but with the departure from U_g in the lower 1000 m such that it will match the non-slip boundary condition at the ground. The main difference between the initial conditions of Experiments I and II is that the latter involves a stronger wind in the boundary layer of the atmosphere.

4. Spatially-averaged predicted quantities

In this and the following two sections, we will present and discuss the results of the two models described in the previous sections. Greater emphasis will be placed on Experiment II because of the more realistic assumptions used in its formulation. Comparison will be made between the experiments in order to demonstrate the dependence of the model upon different parameters and different boundary and initial conditions. Also we will compare the model solutions with observational results, where appropriate, in order to show similarities and differences between the behaviors of the model solutions and the real atmosphere. However, we must emphasize that our initial conditions were chosen to represent mean climatological profiles with no attempt made in this initial study to represent any specific
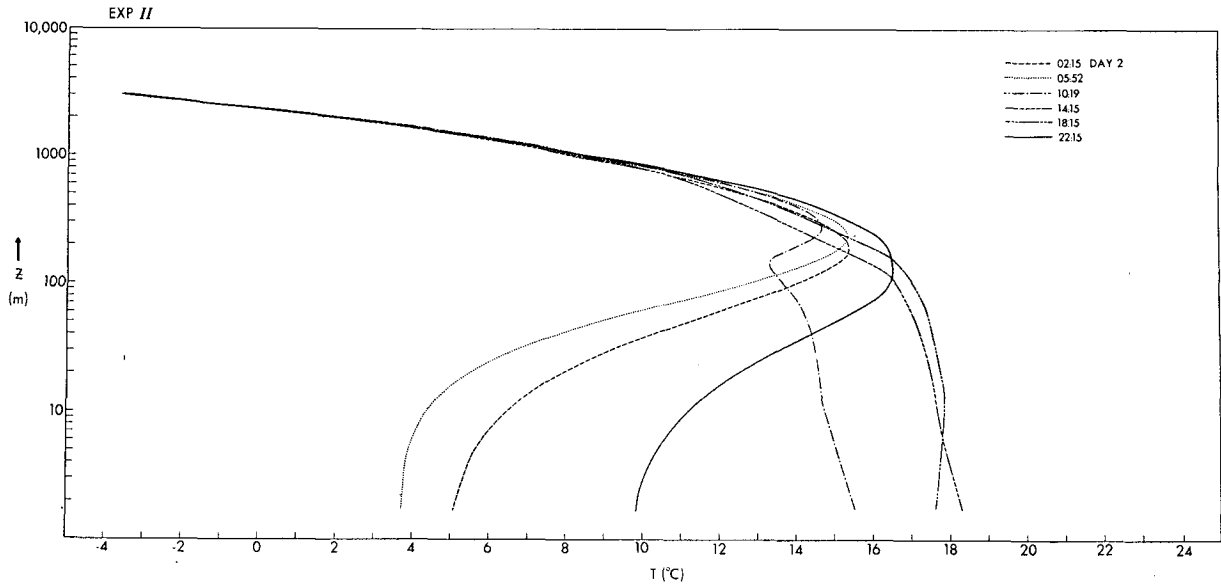
FIG. 2. Temperature profiles at various times (every 4 hr) during Day 2 of numerical Experiment II vs log z.

atmospheric situation. In particular, we will compare our numerical solutions with single-day observations made by Clarke et al. (1971) since we feel that these observations are representative of typical climatological situations.

In this section, we will discuss the time and height variation of mean atmospheric quantities averaged in the x direction along the span L of the model for specific levels in the vertical. These x-averaged results will be comparable with results obtained by many researchers using one-dimensional boundary layer models

(Estoque, 1963; Lykosov, 1972; etc.), but with the obvious advantage that the flux contribution due to larger eddies is computed explicitly in the present model whereas it must be drastically parameterized in the one-dimensional models. Fig. 2 shows the variation of mean temperature with height z over 4-hr intervals during the second day of Experiment II. We note a strong stable temperature gradient over the lower 300 m at 0215. Cooling due to radiation and residual turbulence (generated by the convective activity of the previous day) continues until sunrise as shown by the
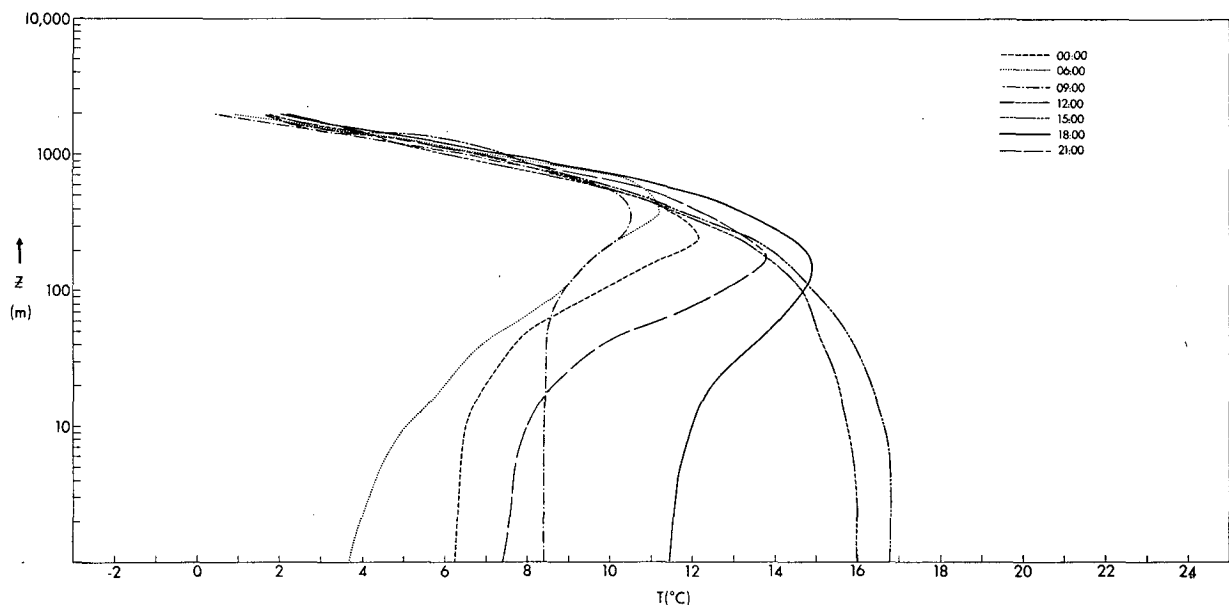

FIG. 3. Observed temperature profiles for 27 July 1967 of the Wangara Experiment (Clarke et al., 1971) vs log z.
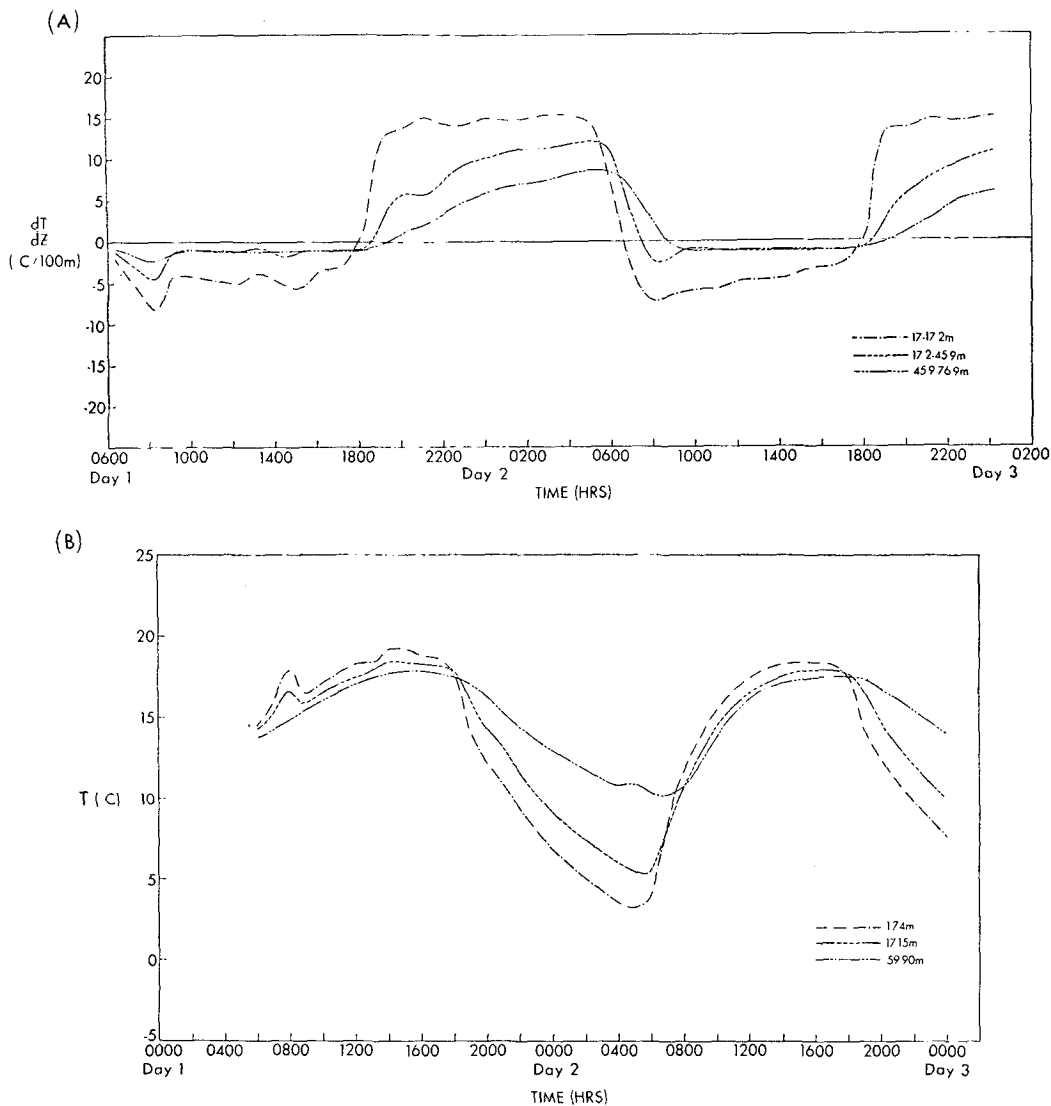
FIG. 4. Lapse rates (a) and temperatures (b) at several levels near the ground in Experiment II.

temperature profile at 0552. After sunrise (0600), the heating at the ground produces a superadiabatic lapse rate near the surface which increases until free convection begins. These thermals then penetrate into the higher stable layers, thereby reducing the stable lapse rate to a neutral one as seen by the successive curves at 1019 and 1415. The occurrence of a stable temperature gradient at the ground in the profile at 1815 reflects the return to cooling at the ground after sunset (1800). This cooling trend continues, producing a temperature structure similar to that of the previous night. The diurnal heating-cooling cycle produces changes in the temperature up to ∼1000 m.

Fig. 3 shows a one-day sequence of temperature profiles over 3-hr intervals from observations made in the Wangara Experiment during quiet synoptic conditions on 27 July 1967 (Clarke et al., 1971). Good agree-

ment can be seen between these results and the model results of Fig. 2 as shown by the general temperature behavior and, in particular, the profiles corresponding to minimum and maximum ground temperature and the height of the penetrative convection layer. It is important to note that times of sunrise and sunset in these winter observations differ from the respective times of 0600 and 1800 used in our model.

The time variation of lapse rate and temperature for three levels close to the ground from Experiments II and Ib is shown in Figs. 4 and 5. In Fig. 4a, we see the initial development of the unstable lapse rate near the ground after 0800 for Day 1 of Experiment II. An anomaly can be seen in the first two morning hours, which appears to be the time required for the superadiabatic lapse rate to become sufficiently unstable to produce thermals which disrupt the stable, quiet initial
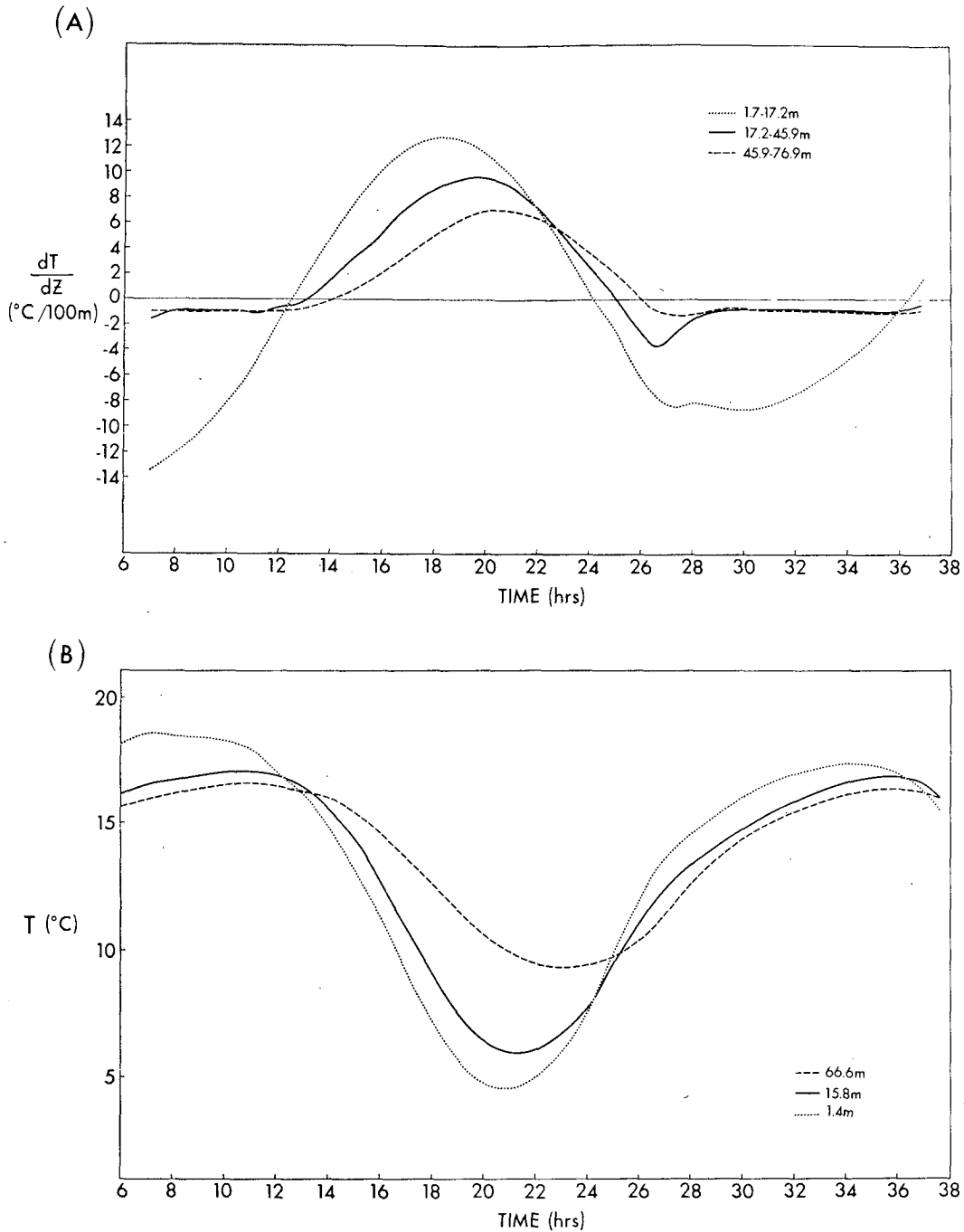
(A)

(B)

Fig. 5. As in Fig. 4 showing lapse rates and temperatures for Experiment I.

stratification above the surface layer. The ensuing free convection rapidly reduces the superadiabatic lapse rates to lower values near the ground and to a dry adiabatic value in the adjacent layers above.

The discrepancy shown between the lapse rate behavior for the first and second daytime periods can be accounted for by the retarding influence in Day 1 of the stable stratification due to our initial conditions. On the other hand, the behavior of the lapse rate during the second day reflects the spread of the turbulence over the fully-developed mixed layer. During the night period between Days 1 and 2, the time behavior of lapse rate between 1.7 and 17 m closely follows the time variation of the heating boundary condition due to the dominance of the constant radiation and background viscosity coefficients. In Fig. 4b, realistic features are shown for the temperature variation at three different levels of the model and, in particular, for

the occurrence of maximum and minimum temperatures at 1500 and 0500 of Day 2, respectively. The relative temperatures for the ground and the 59-m levels compare quite well with those of the Wangara Experiment (shown in Fig. 3).

In Fig. 5a, the lapse rate behavior of the upper two levels for the daytime periods of Experiment Ib shows a strong similarity with that of Experiment II. However, the daytime similarity between the temperature behaviors of the two experiments at the higher levels does not carry over to the lapse rate for the lowest level. Instead, Fig. 5a shows the lapse rate between 1.4 and 17 m following the sinusoidal ground heating function very closely, thereby demonstrating the domination of the constant radiation coefficient R over the eddy coefficient K_H in Experiment Ib. The differences in the nighttime lapse rate behavior and the occurrences of the temperature minima between Experiments II and Ib (Figs. 4b and 5b) reflect the different heating functions used at the lower boundary in these two cases.

Contours of mean hourly temperature are shown in Fig. 6 as a function of height and time for Experiment II. Fig. 7 is a similar plot for the Wangara experiment. Both plots show the shallow stable stratification at night and the deep nearly-neutral stratification during the day. These results seem to be characteristic of a wintertime situation. On the other hand, summer data such as those from the Great Plains Experiment (Lettau and Davidson, 1957) show weaker stratification at night which is caused, we believe, by the large residual turbulence generated during strong penetrative convection during the day.

In order to demonstrate the role of the radiation parameter in our model, we show in Figs. 8a and 8b the nighttime temperature structure from Experiments Ia and Ib with the radiation coefficient R three times
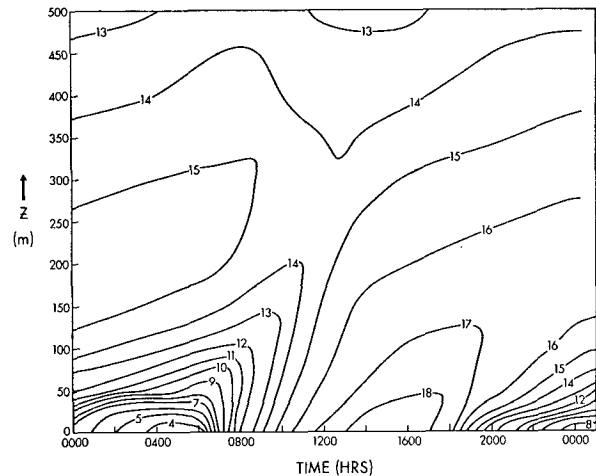

FIG. 6. Height-time contours of mean temperature (°C) averaged horizontally and over $\frac{1}{2}$-hr intervals as calculated for Day 2 of Experiment II.

larger in the latter case. Note that the temperature patterns are virtually identical for the two cases above 75 m but that a much stronger temperature gradient develops near the surface in Experiment Ia at night due to the small value of R in this case. (In Section 6, we will show that radiation effects in our model are only important below 10 m during the day and up to 70 m at night.)

The profiles of mean hourly velocity plotted in Fig. 9 for the second day of Experiment II show a strong diurnal oscillation in the first 1000 m of the atmosphere. Although the velocities at 300 m tend to be maximum at night, the amplitude of the wind oscillation is too small to be considered as a fully-developed low-level
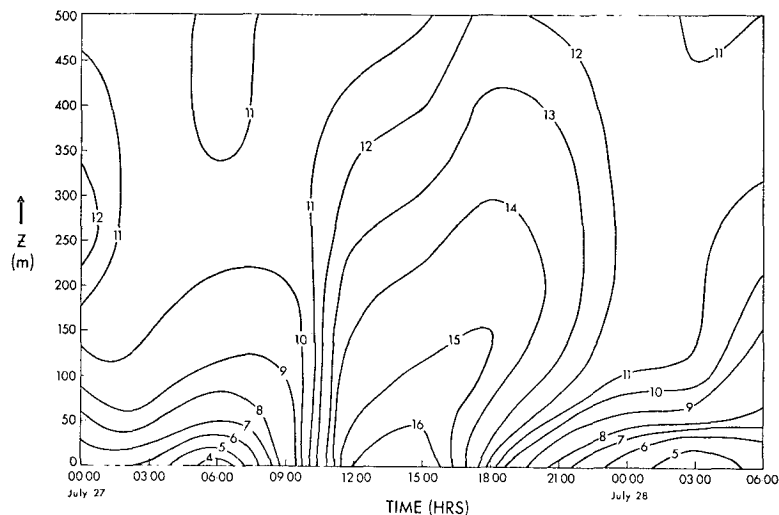

FIG. 7. Height-time contours of temperature (°C) observed at 3-hr intervals on 27–28 July of the Wangara experiment (Clarke et al., 1971).

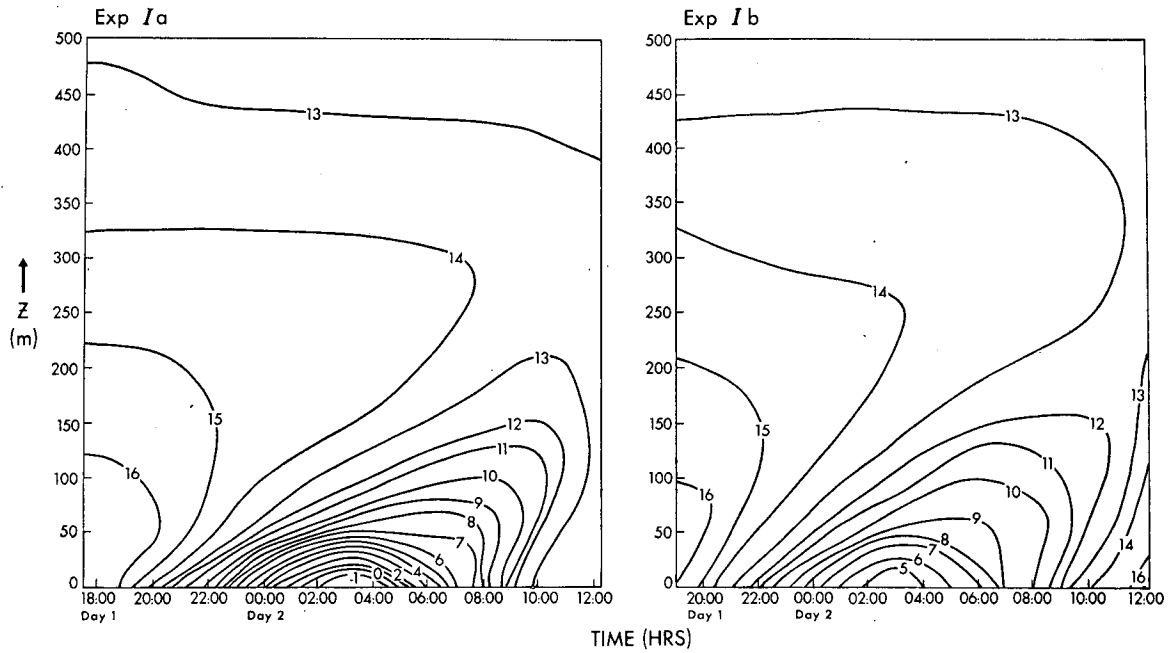FIG. 8. Comparison of nighttime potential temperature contours (°C) for Experiment Ia ($R=0.117$ m² sec⁻¹) and Experiment Ib ($R=0.351$ m² sec⁻¹).
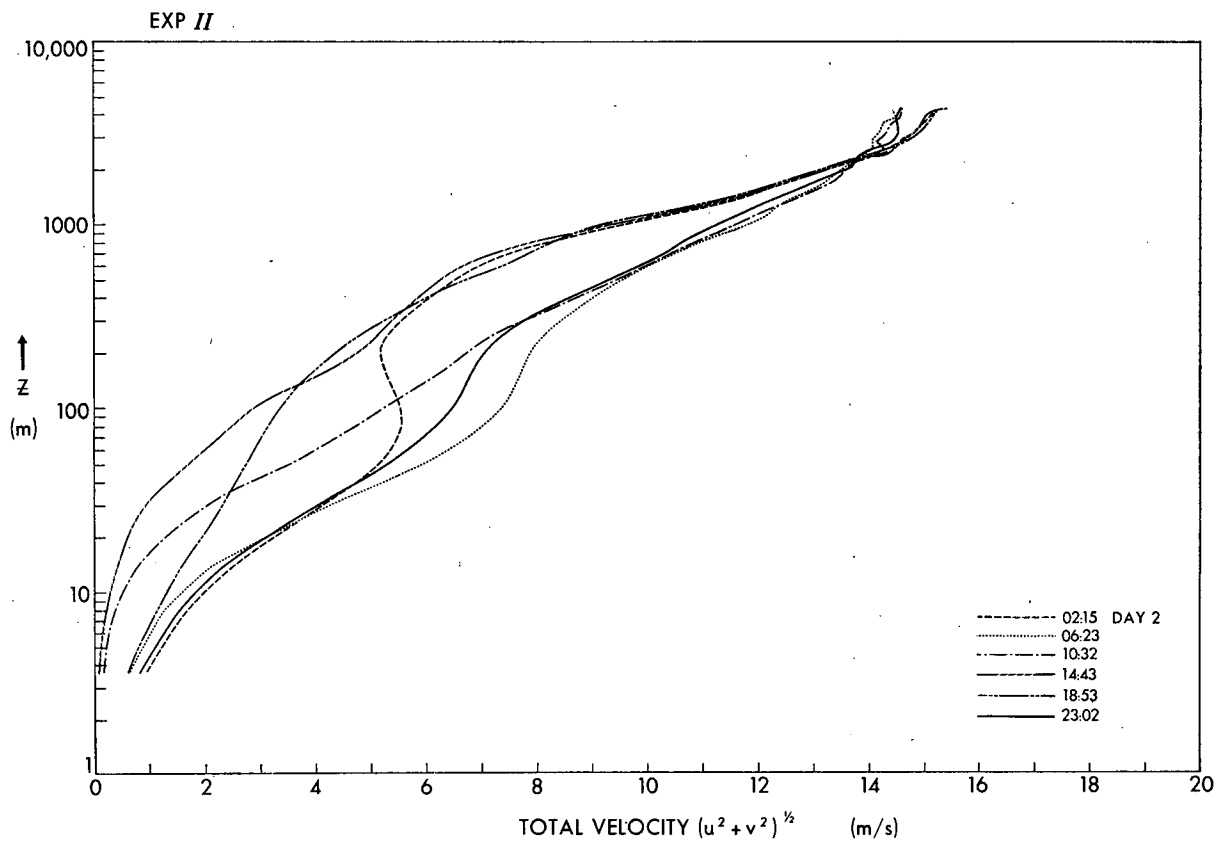
FIG. 9. Profiles of total velocity $(u^2+v^2)^{\frac{1}{2}}$ vs log z for different times from Day 2 of Experiment II.
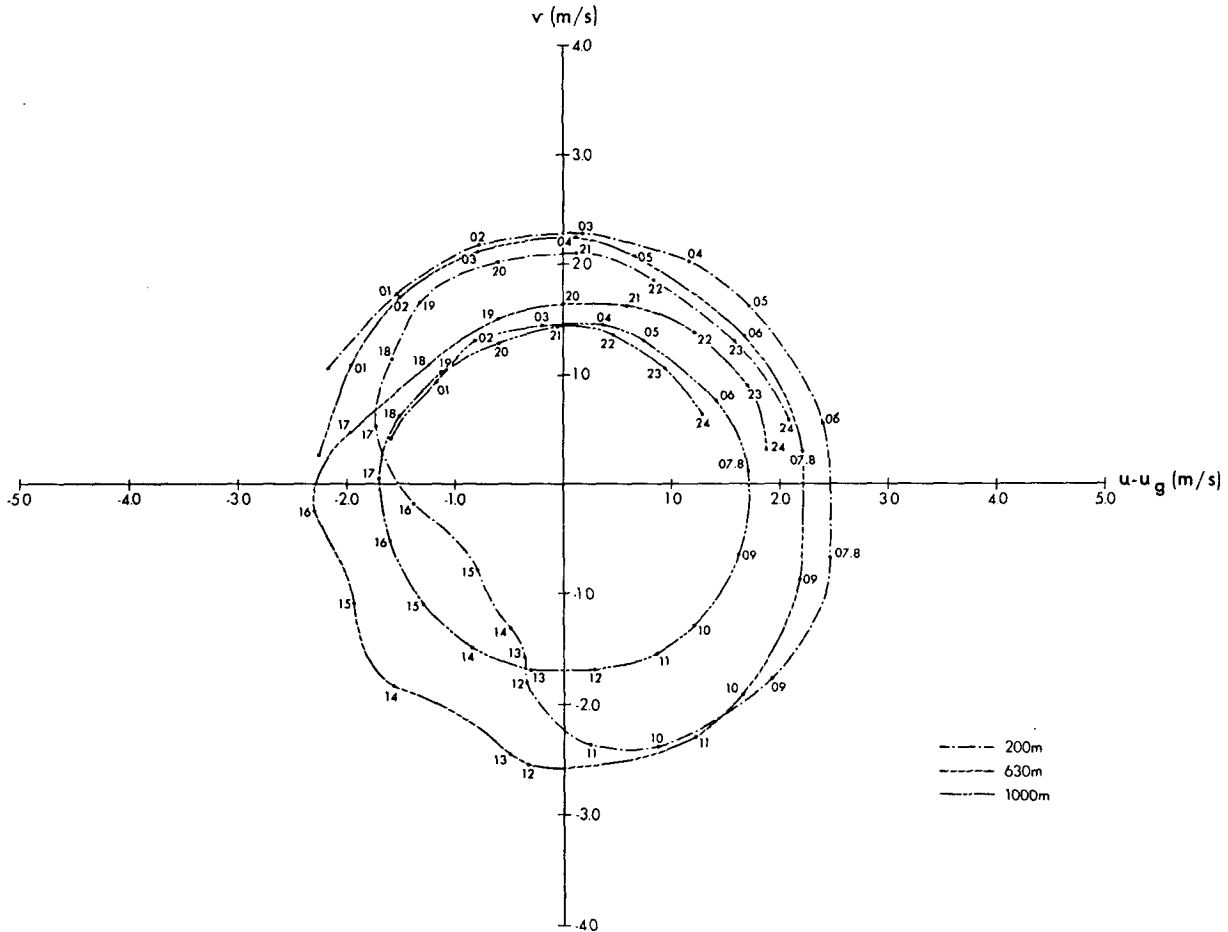
FIG. 10. Hodograph showing difference between mean velocity and the assumed geostrophic wind $U_g(z)$ at three different heights within the planetary boundary layer as a function of time (marked in hours after midnight along each curve) for Day 2 of Experiment II.

jet.[1] Most one-dimensional models show a tendency to reproduce the nocturnal low-level jet by means of inertial oscillations existing in the models (and we cannot reject inertial waves as providing a possible explanation of the low-level jet phenomenon). However, we do not believe that this result provides a conclusive proof that the atmosphere will respond in this way since one-dimensional PBL models have only one degree of freedom for oscillating motions, namely the inertial wave mode, and this mode will be easily excited by any imbalance in the initial conditions of the numerical model. We believe that an alternate explanation is possible, namely that the low-level jet may be caused by a dynamic instability such as the "trapeze" instability proposed by Orlanski (1973); if this is the case, then the formation of this jet will require some four or five days of model time to develop and cannot be expected to produce a well-developed jet after only two days. In fact, mesoscale models which

---

[1] No comparison of velocity profiles was attempted between Experiment II and the Wangara results since our initial conditions were chosen to simulate a general climatological situation rather than any specific observational case.

.are to be used for 24-hr predictions will require prior integration times which are sufficiently long to allow time for those mesoscale processes which require more than one day to develop. An alternate possibility would be to use four-dimensional updating similar to that which has been proposed for use in general circulation prediction models (but obviously with shorter updating time intervals).

In the mixed boundary layer, strong inertial oscillations are generated as shown by the hodograph in Fig. 10 in which the geostrophic wind $U_g(z)$ has been subtracted from the x-velocity component u. There is some evidence of these oscillations in the PBL (Hess and Clarke, 1973). These inertial waves may be one of the most important characteristics of the so-called Ekman boundary layer where they will be excited by transient mixing due to the diurnal cycle.

5. Time and space variation of the predicted quantities

The behavior of the x-averaged atmospheric quantities as described in the previous section will depend to
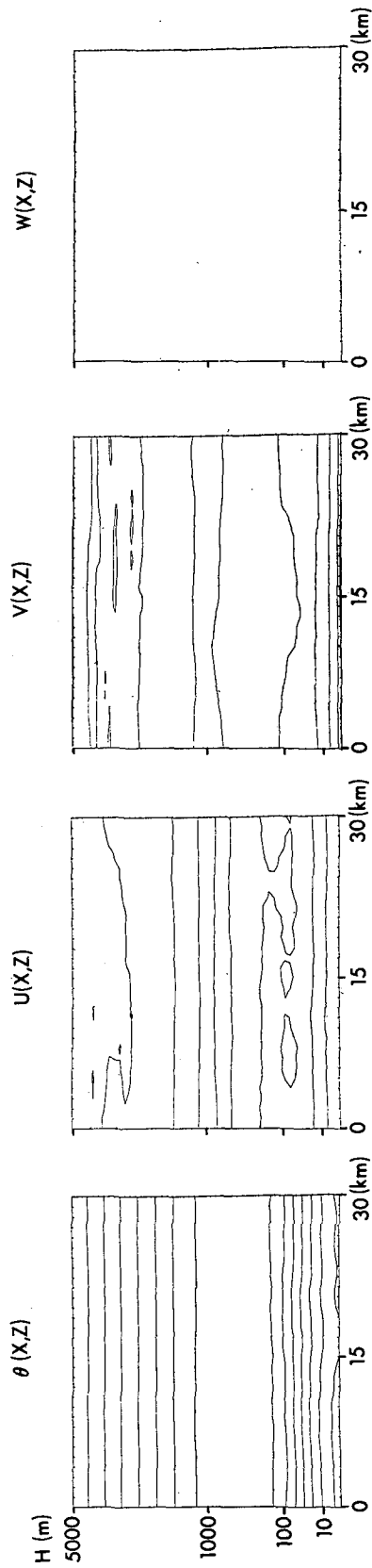
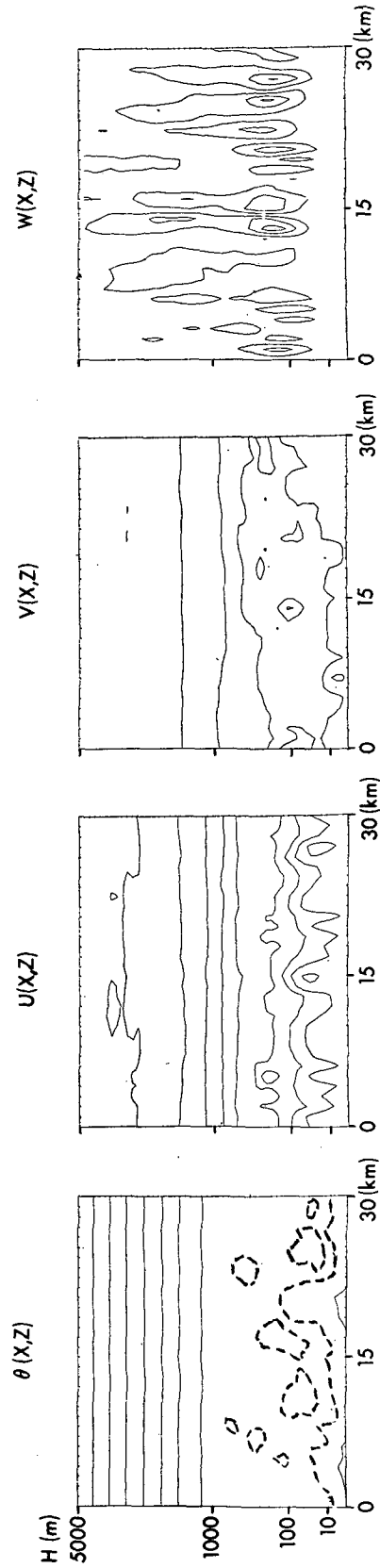FIG. 11. Typical contour plots of potential temperature θ and velocity components u, v, w for nighttime (0232, Day 2) and daytime (1446, Day 2) conditions from Experiment II. Contour intervals for θ, u, v, w are 2C, 2.0 m sec^{-1}, 1.0 m sec^{-1} and 0.125 m sec^{-1}, respectively. Several dashed temperature contours are added to the daytime θ plot to show the temperature structure in the well-mixed convection region.
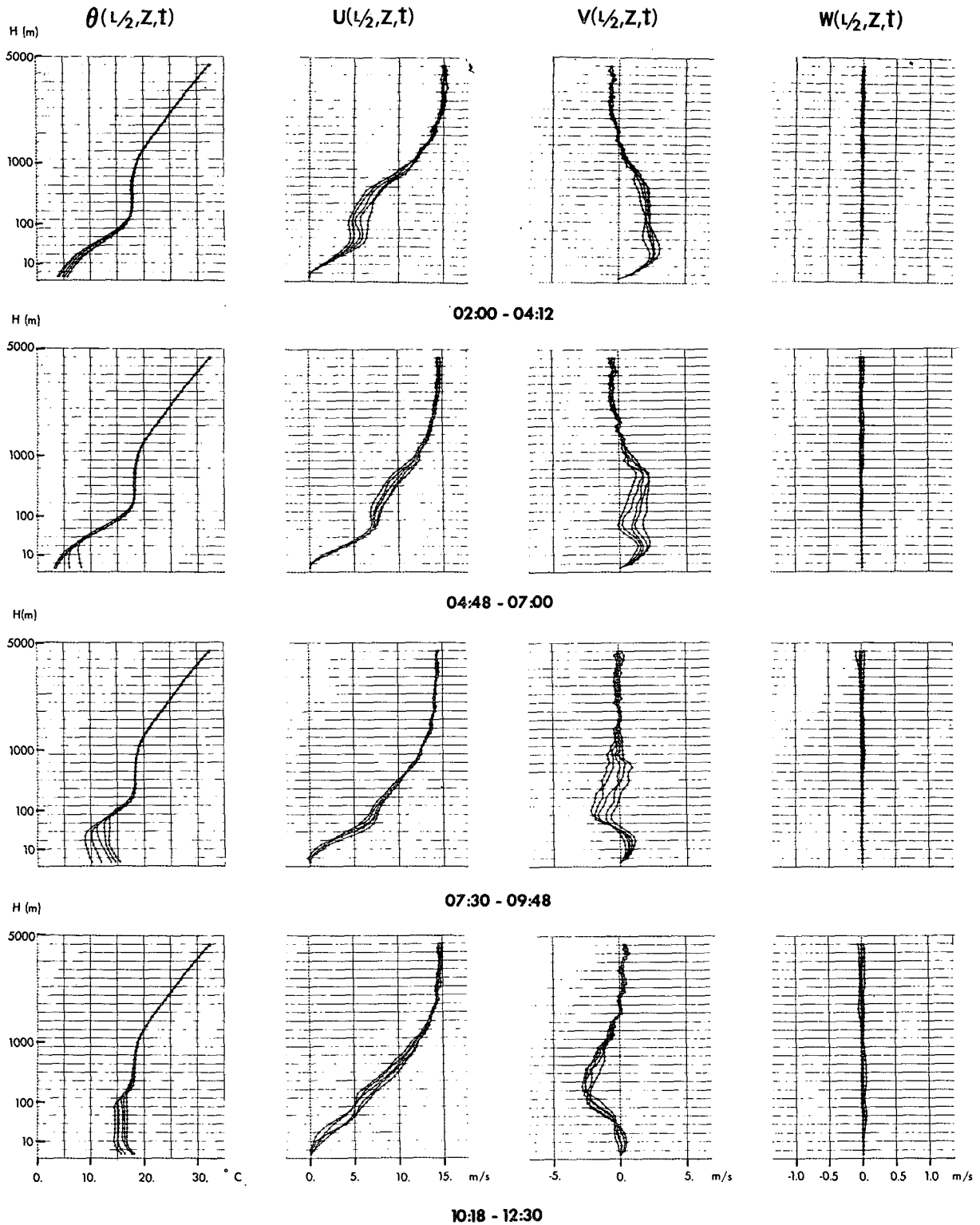
FIG. 12. Profiles of θ, u, v, w for the horizontal station $x = L/2$ vs log z for 0200 to 1230 of Day 2 of Experiment II. Each individual curve represents the profile of the quantity averaged over a model time interval of 2000 sec (200 time steps).

a large extent upon spatially-varying phenomena such as convection eddies and internal gravity waves. In-

deed, the vertical transport of heat and momentum in the turbulent atmosphere is achieved by means of tur-

θ(L/2,Z,t)   U(L/2,Z,t)   V(L/2,Z,t)   W(L/2,Z,t)

13:06 - 15:18
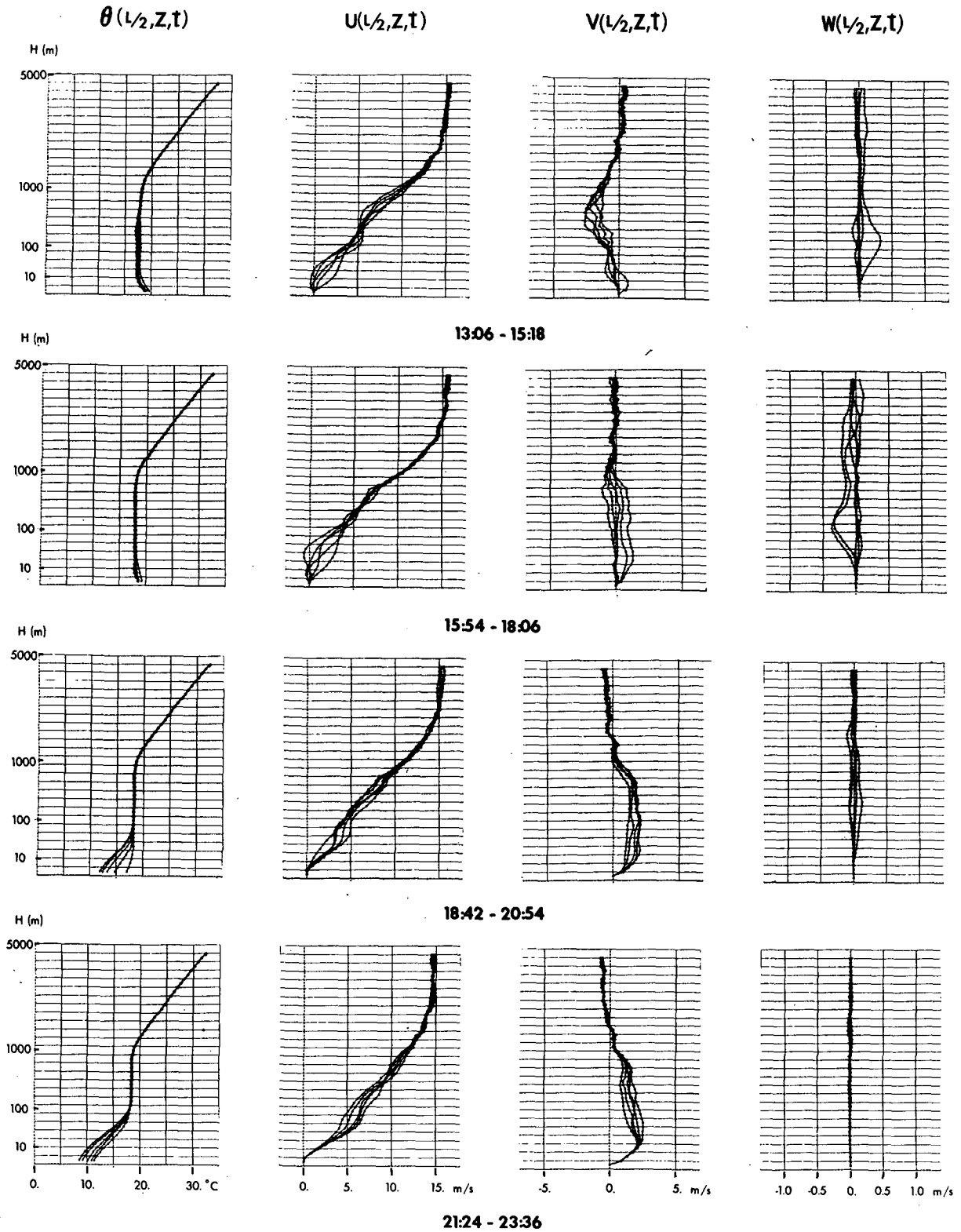
15:54 - 18:06

18:42 - 20:54

21:24 - 23:36

FIG. 13. As in Fig. 12 except for 1306 to 2336 of Day 2.

bulent eddies which are inherently three-dimensional. Although the eddy viscosity parameterization described

earlier and included in the model simulates transfer processes due to subgrid-scale eddies, the eddies which
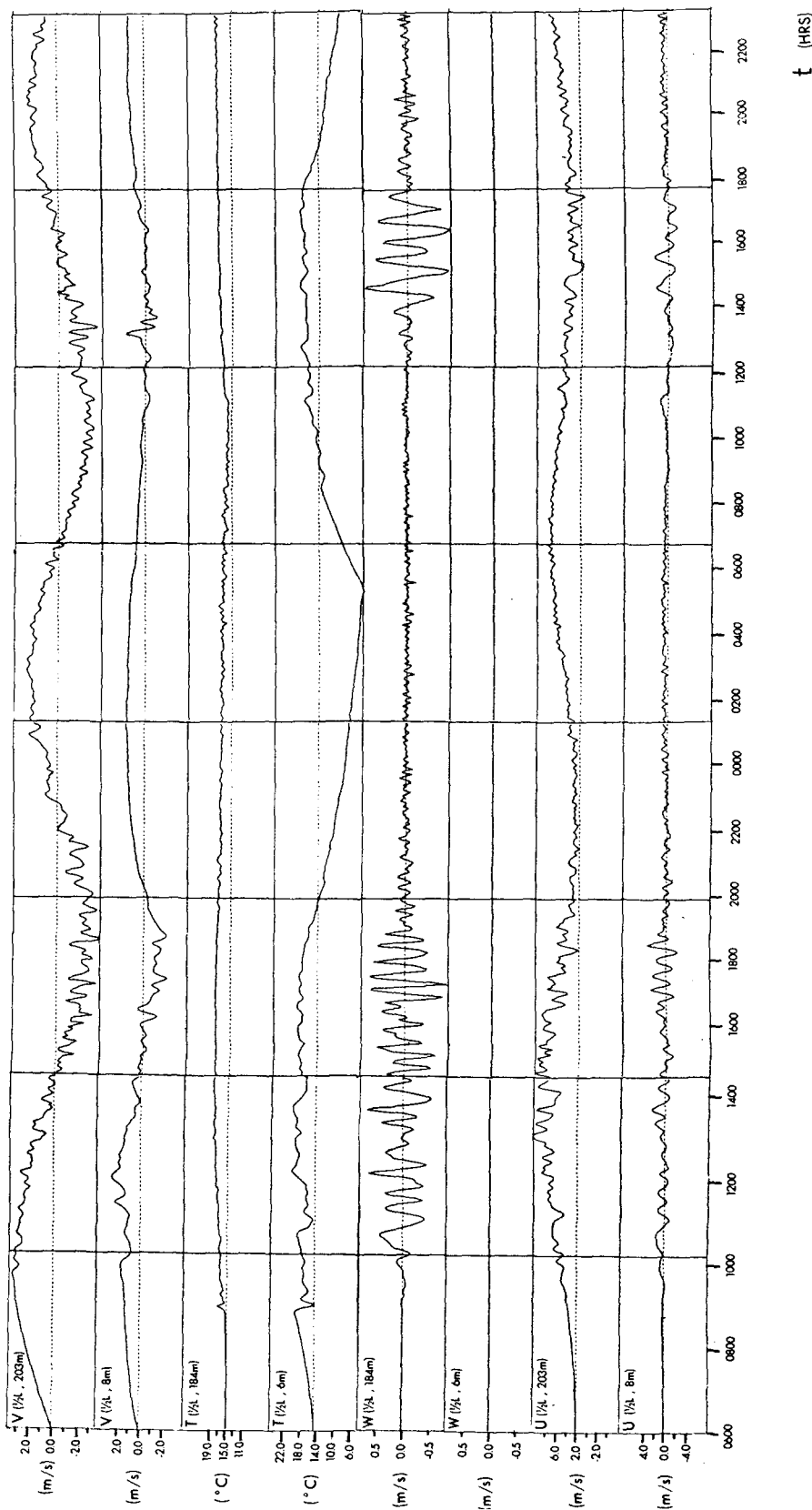
FIG. 14. Time variation of point values of temperature T and velocity components u, v, w at the horizontal station $x=L/2$ from Experiment II. Horizontal velocity components u and v are shown for heights of 8 and 203 m while temperature and vertical velocity component w are given for heights of 6 and 184 m. Values used to construct these curves represent 200-sec (20 time steps) averages.
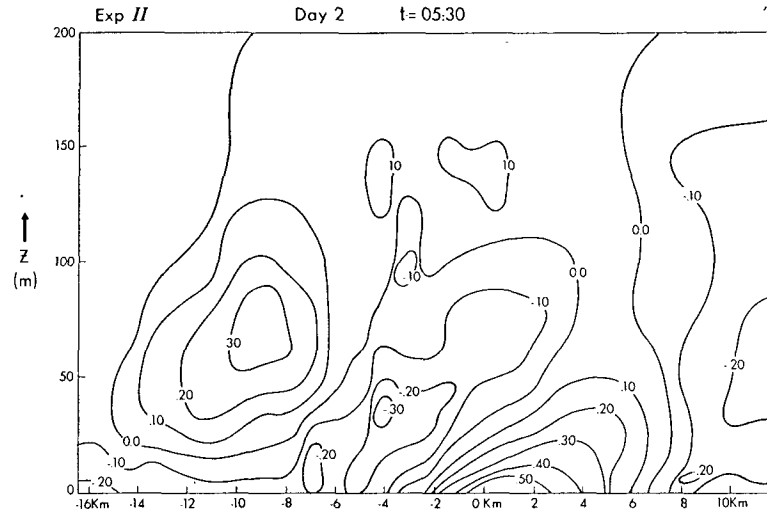
FIG. 15. Contour plot of $\theta - \bar{\theta}(z)$, the perturbation of local potential temperature from its horizontally-averaged value, for 0530 of Day 2 of Experiment II. The figure shows a heat island effect due to the minimum cooling (see Fig. 1 and Table 1 showing the imposed heat flux distribution at the ground) at $x - L/2 = 0$ km.

are resolved by the model play a vital role in transferring heat and momentum above the first 10 m of the surface (as will be shown in Section 6). Typical daytime and nighttime situations for Experiment II are shown by the contour plots in Fig. 11 of the spatial variation (up to 5000 m) of temperature and the three velocity components. Note that the vertical coordinate z is stretched according to the log-linear function $Z(z)$ given in Table 1 for Experiment II. This distortion was done purposely in this figure in order to increase the detail of the lower boundary layer. The most striking aspect of this figure is the increased eddy activity in the daytime (lower part of Fig. 11) as compared to the nighttime (upper part). Most of the other features related to the variation of mean quantities have been discussed in the previous section.

The high wavenumbers which are evident in Fig. 11 are due to free convection processes which tend to choose shorter horizontal scales. Clearly, we cannot claim good resolution for individual thermals with $\Delta x = 1$ km. However, since the time and vertical variation of these waves is well resolved as will be seen in the following figures, we believe that the collective effect of the vertical transfer of heat and momentum by these waves is modeled fairly realistically. Likewise, since the net horizontal transport due to eddies is far smaller than the vertical transport in our model (typical Δz near the ground is 5 or 10 m compared to the 1 km horizontal grid size), the lack of horizontal resolution does not appear to be crucial.

In order to display the time variation of the local quantities shown in Fig. 11, we have plotted in Figs. 12 and 13 a sequence of profiles of the local values of the potential temperature and the velocity components as taken from the solution at the horizontal station

$x = L/2$. Each profile represents a time average over an interval of 33 min. The vertical velocity profiles from 1300 to 1836 show the vertical scale of the eddies to be of the order of several hundred meters. An interesting feature is the progression of the local potential temperature profiles from night to day, and, in particular, the abrupt changes from 1018 to 1306 due to the strong convective activity.

To emphasize the temporal behavior of these eddies, we have plotted, in Fig. 14, the time variation of v, θ, w and u for two different levels, with $z = 203$ and 8 m for v and u and $z = 184$ and 6 m for θ and w. Again, the maximum activity is found during the day with the period of typical oscillations being ~ 30 min (200 time steps). The maximum vertical velocity at 200 m is about 50 cm sec^{-1} which seems to be reasonable for the eddy scales which are resolved by our model.

Finally, before ending this section, we should mention something about the atmospheric effects due to the x variation of our heating function. Our secondary motivation in this paper was to investigate the effect on the atmosphere of a heat source similar to that produced by a city. The amplitude of the heat source used is small compared with the heating observed for a typical city. This was done purposely because we felt that the periodic boundary conditions used here would strongly affect the development of a large heat island. However, a tendency toward the formation of a heat island can still be observed as shown by the plot in Fig. 15 of the contours of $\theta - \bar{\theta}(z)$ from Experiment II at 0500. Note the heat dome which has formed over the center of the heat anomaly and tilts to the right due to the effect of the wind shear. [This effect is similar to the heat island plume observed by Clarke (1969) and modeled in several different numerical experiments
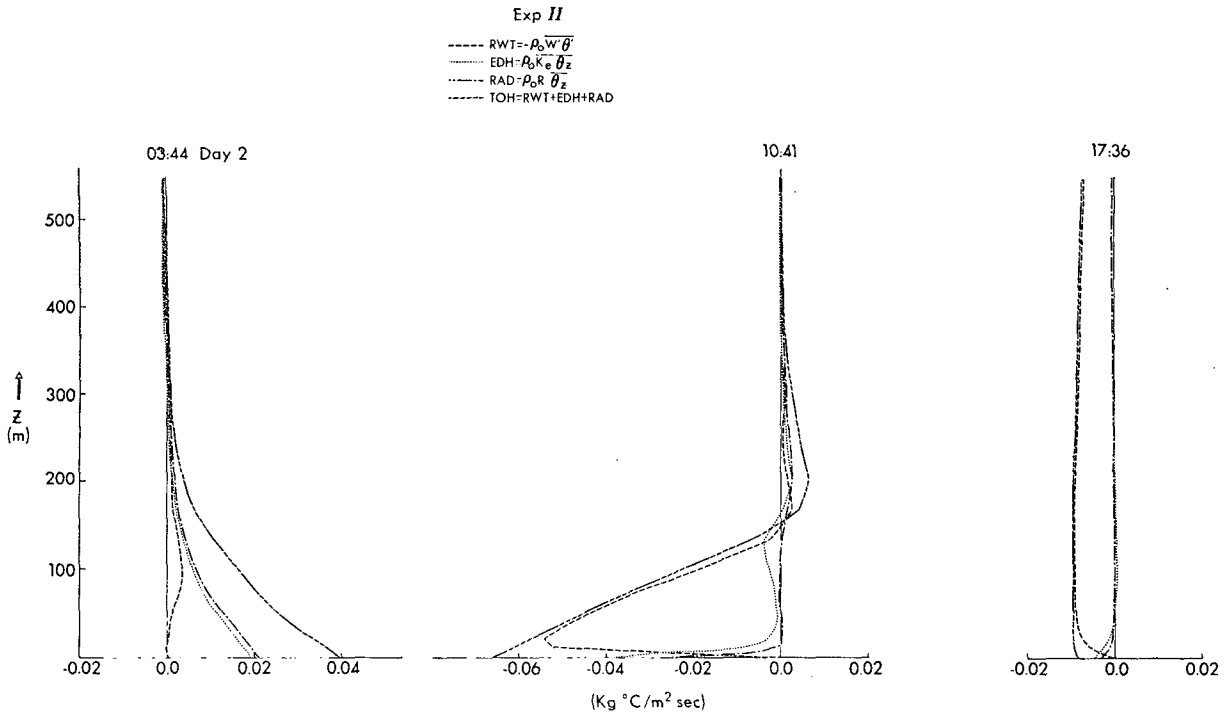
Exp *II*

```
----- RWT=-ρ₀w'θ'
........ EDH=-ρ₀Kₑ θ̄z
----- RAD=-ρ₀R θ̄z
----- TOH=RWT+EDH+RAD
```


FIG. 16. Profiles of total vertical heat flux TOH as well as resolved sensible flux RWT, parameterized sensible flux RWT, parameterized sensible flux EDH, and radiative flux RAD for 0344, 1041 and 1736 of Day 2 of Experiment II.

Exp *II*

17:36 hr Day 2
```
----- (TOX²+TOY²)½
........ TOY
---·--- EDY
----- RVW
---·-- TOX
----- EDX
--·-- RUW
```
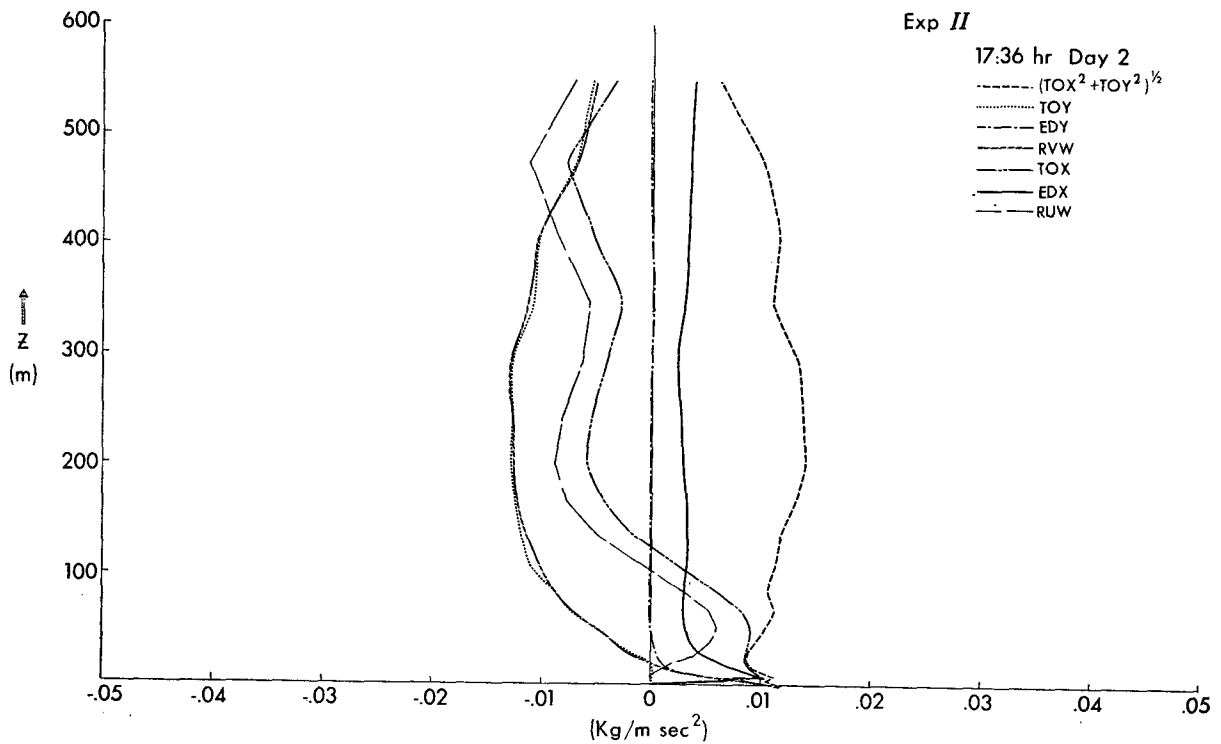
FIG. 17. Profiles of the magnitude of the total vertical momentum flux as well as the individual x and y components TOX and TOY and the resolved flux components RUW and RVW and the parameterized flux components EDX and EDY, all for 1736 of Day 2 of Experiment II.

(e.g., McElroy, 1972)]. The height of this dome is ~60 m which is considered to be shallow for an urban heat island dome. The maximum difference between "city" and "country" surface temperatures is ~0.8C, a difference which seems reasonable in view of the small heat source used.

An interesting feature shown in this figure is the occurrence of alternate regions of low and high temperatures occurring upstream of the dome. We believe that these anomalies are not due to the cyclic boundary conditions but rather are due to physical effects which can be explained as follows: The heat island has a blocking effect on the winds near the surface. This blocking produces an upward vertical velocity upstream of the heat dome which lifts colder air from the surface to produce relatively lower temperatures at higher levels in the boundary layer. Consequently, a downward motion occurs farther upstream of this region of upward motion with warmer air being carried downward to produce the warm region shown.

6. Boundary layer dynamics

The proper representation of the dynamics of the boundary layer is crucial to the successful simulation of mesoscale dynamics, particularly when the physics of interest is driven by energy sources at the surface. In this section, we will look more closely at the behavior of those quantities which control the boundary layer dynamics.

One of the most · important quantities governing these processes is the vertical eddy fluxes which are obtained by horizontally averaging the momentum and heat equations (2.1) and (2.3). The predominant terms obtained from such averages when the flow is nearly steady involve the Reynolds stress terms in the momentum equations and the eddy flux and the radiation terms in the temperature equation. The Reynolds stress and the eddy heat flux terms occur in two forms in the equations: first as explicit covariance terms and second as parameterized flux terms. The covariance terms for the vertical eddy heat flux RWT and the x and y components of the vertical Reynolds stresses RUW and RVW are defined as

$$
\left.\begin{array}{l}
RWT = -\rho_0 \overline{w'\theta'} \\
RUW = -\rho_0 \overline{u'w'} \\
RVW = -\rho_0 \overline{v'w'}
\end{array}\right\},
$$

where primes designate perturbations from the current horizontally-averaged mean values. (We have dropped the constant specific heat coefficient c_p which should be included in the heat flux terms to make them dimensionally correct.) Similarly, the parameterized forms of the vertical eddy heat flux EDH and the x and y components of the vertical Reynolds stresses EDX

and EDY are defined as

$$
\left.\begin{array}{l}
EDH = \rho_0 K_e \overline{\dfrac{\partial \theta}{\partial z}} \\[2ex]
EDX = \rho_0 \nu_e \overline{\dfrac{\partial u}{\partial z}} \\[2ex]
EDY = \rho_0 \nu_e \overline{\dfrac{\partial v}{\partial z}}
\end{array}\right\},
$$

where z derivatives have been put into the proper finite-difference form in the analysis of the numerical solution. (Note that K_e and ν_e are included under the averaging bar because of their possible variation in space and time.) Finally, the radiative flux RAD is defined as

$$
RAD = \rho_0 R \overline{\frac{\partial \theta}{\partial z}},
$$

where we need only consider the vertical gradient of the average temperature because the radiation coefficient R was taken as constant. In the discussion which follows, we shall refer to the total heat flux TOH and the total x and y components of Reynolds stresses TOX and TOY which we define as

$$
\left.\begin{array}{l}
TOH = \rho_0 K_e \overline{\dfrac{\partial \theta}{\partial z}} - \rho_0 \overline{w'\theta'} + \rho_0 R \overline{\dfrac{\partial \theta}{\partial z}} \\[2ex]
TOX = \rho_0 \nu_e \overline{\dfrac{\partial u}{\partial z}} - \rho_0 \overline{w'u'} \\[2ex]
TOY = \rho_0 \nu_e \overline{\dfrac{\partial v}{\partial z}} - \rho_0 \overline{w'v'}
\end{array}\right\}.
$$

Fig. 16 shows the vertical profiles of the heat fluxes over the lower 500 m from Experiment II at 0344, 1041 and 1736 of Day 2. The nighttime profiles (0344) are characterized by a very weak eddy flux RWT with a maximum at around 100 m. The predominant terms are seen to be EDH and RAD, showing an excess cooling in the levels below 300 m.

Several hours after sunrise (1041), the direction of the fluxes is reversed in the lower 150 m. In this situation, the radiation and parameterized eddy flux are predominant in the lowest 10 m. Above this level, the eddy heat flux RWT becomes the most important mechanism for heat transfer. As discussed previously, the turbulent layer becomes deeper as the day progresses, thereby extending the effect of the eddy heat flux RWT to about 1000 m as shown in the last set of profiles (1736) of Fig. 16.

The results shown in Fig. 16 are in apparent conflict with the general belief (with inconclusive observation
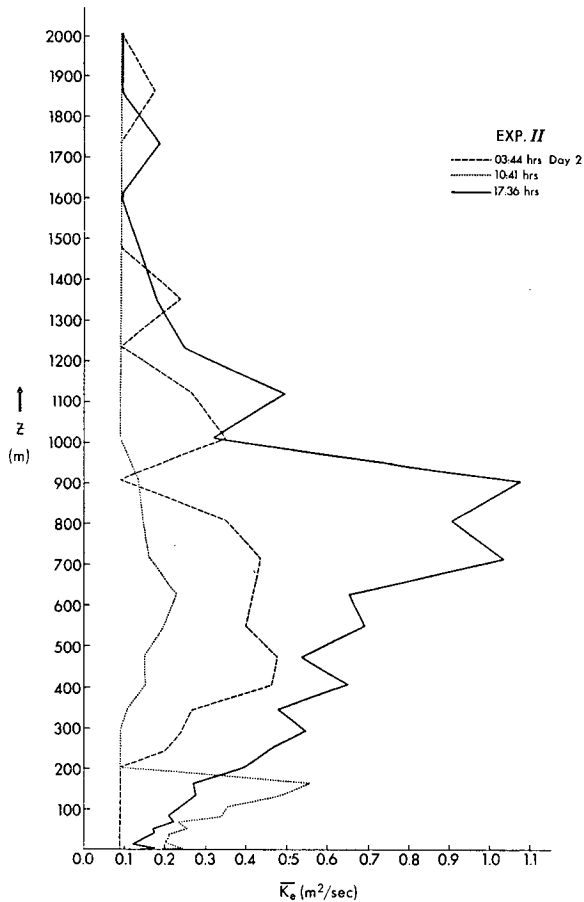
EXP. *II*

------- 03·44 hrs Day 2
············ 10·41 hrs
———— 17·36 hrs

FIG. 18. Profiles of horizontally-averaged values of the parameterized eddy diffusivity K_e for three different times during Day 2 of Experiment II.

evidence) of the constancy of heat flux with height for the lower 50 m of the atmosphere throughout the day. In fact, the constant flux layer may be defined more precisely as the layer in which the vertical integral of the time variation of temperature over the layer is small compared to the magnitude of the heat flux. Lumley and Panofsky (1964) chose this criterion to be less than 20%. Under this criterion, the numerical results shown in Fig. 16 give a constant flux layer 50–100 m deep during most of the day. However, Fig. 16 shows that a deep constant flux layer occurs only in the late afternoon. This behavior can be explained by the fact that the time variation of the integrated temperature over this column is minimum at this time of the day. Fig. 4 shows that temperature over the first 50 m is approximately constant in time for the last 3 hr prior to sunset. Only during this period can we expect conditions which strictly justify a constant flux layer, in agreement with the results shown in Fig. 16.

In a like manner, the x and y components of the stresses as well as the total stress amplitude are shown in Fig. 17 for the lower 600 m of Experiment II at

1736 of Day 2. The momentum flux results are shown for this time of day because our previous discussion of heat flux results suggested that constant flux conditions are most likely to be found in our model during the late afternoon. The figure, in fact, shows the amplitude of total stresses to be constant with height; however, the phase angle between the two stress components TOX and TOY is not constant with height. As in the previous figure, the eddy stresses RUW and RVW provide the principal means of momentum transfer above 50 m. Below 25 m, the parameterized stresses EDX and EDY are predominant as expected since the vertical velocity as well as the eddy stresses must go to zero at the ground.

The x component of the parameterized stress is seen in Fig. 17 to drop to unrealistically small values in the lowest two levels of the model. This result, which is caused by the bad behavior of the x-velocity component u near the ground, may be related to the fact that the model only computes the y-velocity component v and the vorticity ζ in the x-z plane. The constraint on the x- velocity u which is imposed by the vorticity boundary condition (3.6) is apparently too weak to produce a logarithmic wind profile close to the ground. In fact, this bad behavior of u will also be apparent in the discussion of the universal functions ϕ_m and ϕ_H computed from the numerical results, which will be discussed later in this section.

It is interesting to show the actual behavior of the parameterized eddy diffusion coefficient (2.8) as a function of height for three different times of the day. The profiles of the horizontally-averaged values of K_e are shown in Fig. 18. The characteristic night profile (0344) shows $\bar{K}_e$ to equal the background value K_0 in the lower 200 m due to the stable conditions (as shown in Fig. 12). Above this layer, the increase in $\bar{K}_e$ implies that turbulence is still present at night. Although the mean stratification in these layers is stable on the average, the dependence of $\bar{K}_e$ on local unstable temperature gradients caused by eddy activity in these layers produces a net increase in the total eddy diffusivity over its background value K_0. This eddy activity decreases through sunrise with this decrease in $\bar{K}_e$ above 200 m being apparent in the profile at 1041. On the other hand, this morning profile shows an increase in $\bar{K}_e$ below 200 m due to the unstable conditions caused by surface heating after sunrise. The height of this region corresponds to the height of the penetrative convection layer at this time of the day. As the day progresses, the effect of convection penetrates deeper (up to 1000 m), with the eddy diffusivity increasing in a like manner as shown by the late afternoon profile (1736) in Fig. 17.

The maximum values for $\bar{K}_e$ are seen to be very small (<1 m^2 sec^{-1}) compared to values estimated for the real atmosphere. However, if we define a total eddy diffusivity $\bar{K}_T = -(\overline{w'\theta'}/\theta_z) + \bar{K}_e$, which includes the effects of the eddy flux RWT as well as the parameter-

TABLE 2. Comparison of average values of parameterized eddy diffusivity $\bar{K}_e$ and total effective eddy diffusivity $\bar{K}_T$ (units=m² sec⁻¹) at two different heights for three representative times during Day 2 of Experiment II.

Z (m)	0300		1000		1700	
	$\bar{K}_T = \dfrac{-\overline{w'\theta'}}{\bar{\theta}_z} \pm \bar{K}_e$	$\bar{K}_e$	$\bar{K}_T = \dfrac{-\overline{w'\theta'}}{\bar{\theta}_z} + \bar{K}_e$	$\bar{K}_e$	$\bar{K}_T = \dfrac{-\overline{w'\theta'}}{\bar{\theta}_z} + \bar{K}_e$	$\bar{K}_e$
100	0.1	0.09	20	0.35	95	0.23
400	−2.7	0.44	0.6	0.15	100	0.63

ized flux EDH, we obtain the more realistic values shown in Table 2 which shows values of $\bar{K}_T$ and $\bar{K}_e$ at two heights for the three chosen times of the day. At 100 m, the table shows K_T and K_e at night, a result which agrees with the low level of eddy activity at this time as shown in Fig. 16; on the other hand, daytime values show the strong influence of the convective activity with K_T reaching values of the order of 100 m² sec⁻¹. Similar values are reached at 400 m

during the day. However, a countergradient heat flux occurs at this level during the night. This effect is attributable to the fact that this region is only slightly stable in the mean and thus will allow vertical advection of heat in local regions of unstable stratification to produce a net countergradient heat flux.

The unsteady behavior of eddy activity at different times of the day can be seen by the plot in Fig. 19 of contours of sensible heat flux EDH+RWT [in units
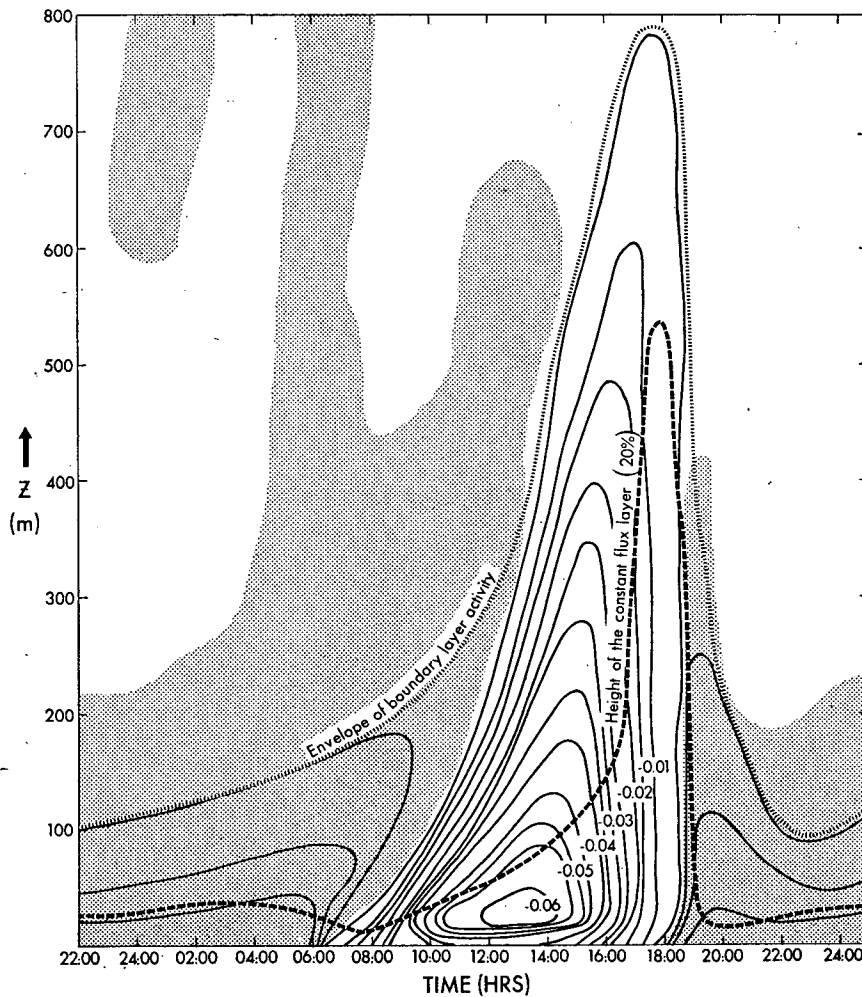

FIG. 19. Contour plot of the time variation of the sensible vertical heat flux EDH and RWT [kg (°C) (m² sec)⁻¹] in the planetary boundary layer for Day 2 of Experiment II. Shaded areas denote downward heat flux while unshaded areas specify upward heat flux. Definitions of the constant flux height and the envelope of boundary layer activity are given in the text.
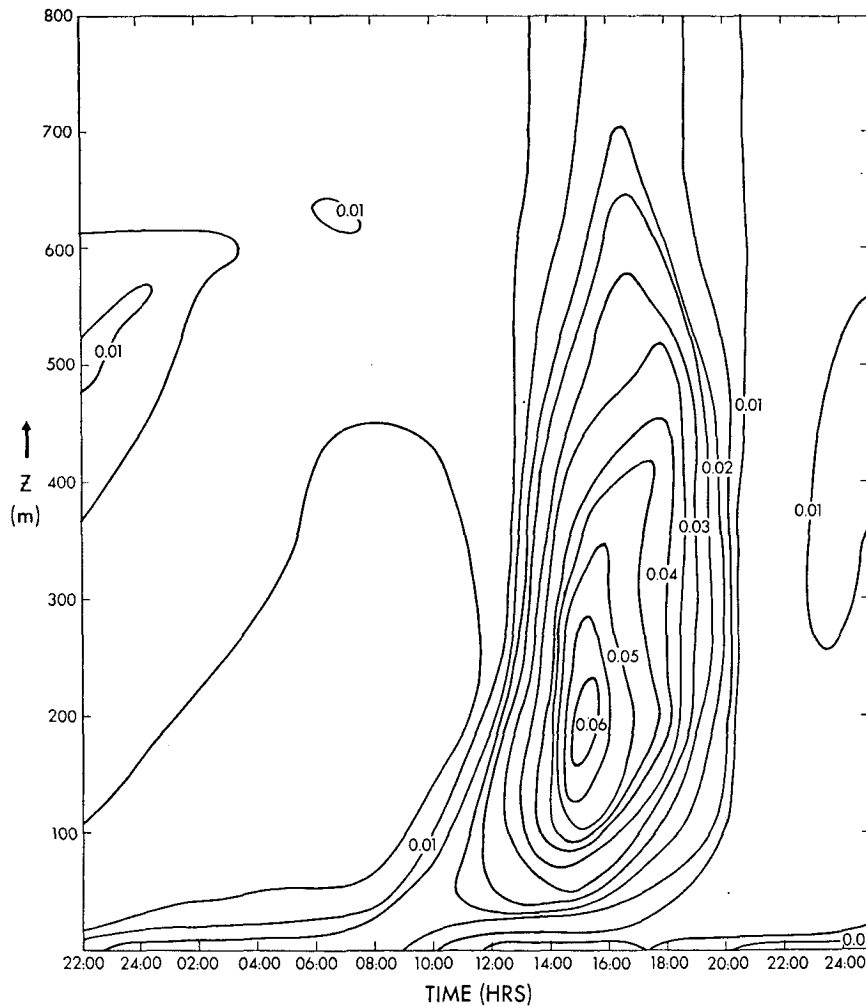
FIG. 20. Contour plot of the time variation of the magnitude of the vertical momentum flux $(\text{TOX}^2+\text{TOY}^2)^{\frac{1}{2}}$ [kg (m sec^2)$^{-1}$] for Day 2 of Experiment II.

of kg (°C) (m^2 sec)$^{-1}$] as a function of height and time. The height of the constant flux layer is seen to be minimum after sunrise and sunset with a sharp maximum of $\sim$500 m occurring late in the afternoon as was discussed above. Also we have sketched in this figure the approximate envelope of boundary layer activity as prescribed by the line above which vertical heat fluxes are less than 0.005 kg (°C) (m^2 sec)$^{-1}$, or less than 10% of the maximum daytime heat flux. This envelope shows that the effective boundary layer height changes from 100–200 m at night when conditions are quiet, to the order of a kilometer during the day because of the strong convective activity.

An analogous contour plot of the amplitude of momentum flux as a function of time is shown in Fig. 20. The mid-afternoon occurrence of maximum momentum flux activity agrees with the heat flux results of Fig. 19 as one would expect. The peak momentum flux occurs at $\sim$200 m above the ground.

Up to this point, we have been discussing the behavior

of the numerical solution of the planetary boundary layer as a whole. However, most observational data are confined to the surface boundary layer (typically consisting of the lowest 10 m); these observations (Businger et al., 1971, and others) confirm the validity of the Monin-Obukhov universal functions ϕ_m and ϕ_H which are only dependent upon the height z non-dimensionalized by a characteristic length L_m. This length scale L_m is defined as

$$L_m \equiv \frac{u^{*3}}{kg\dfrac{H}{\theta_s}}, \qquad (6.1)$$

where

$$u^* \equiv (\text{TOX}^2+\text{TOY}^2)^{\frac{1}{2}}/\sqrt{\rho_s} \qquad (6.2)$$

is the friction velocity, H the surface heat flux, ρ_s and θ_s are the density and temperature at the ground, and k the von Kármán constant (taken here to equal 0.40).
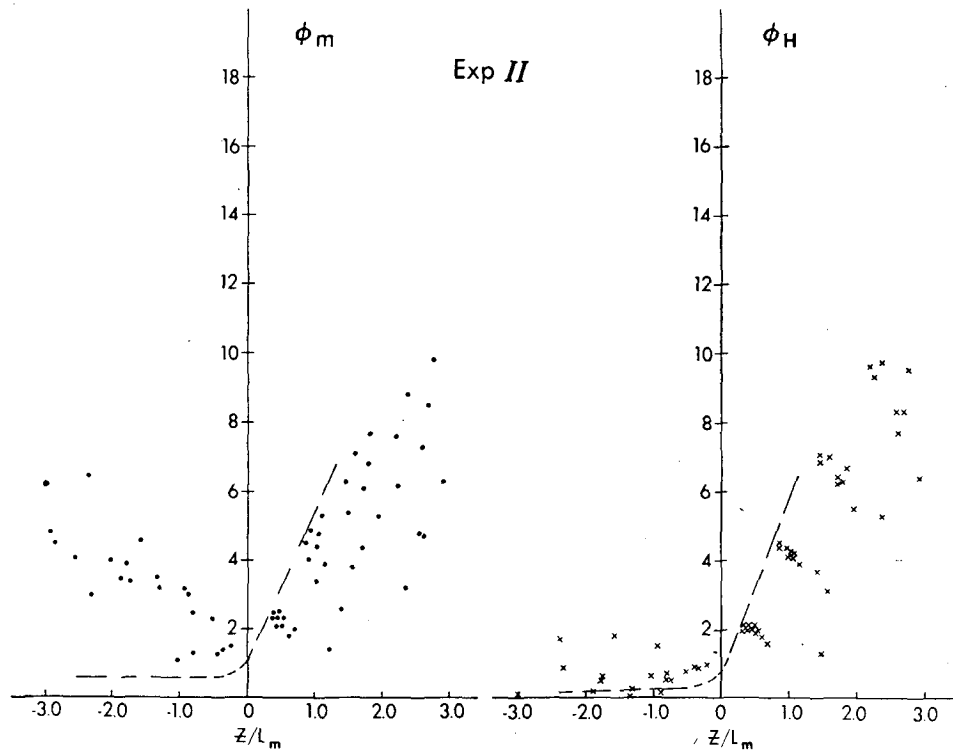
Fig. 21. Plot of nondimensional vertical shear ϕ_m and vertical temperature gradient ϕ_H vs height ratio z/L_m (see text for definitions) from observational data of Businger *et al.* (1971) (dashed line) and computed results of Experiment II (dots and crosses).

Then ϕ_H is the nondimensional vertical temperature gradient and ϕ_m the nondimensional vertical shear, defined as

$$\phi_H \equiv \frac{k(z+z_0)u^*}{H} \frac{\partial \theta}{\partial z}, \qquad (6.3)$$

$$\phi_m \equiv \frac{k(z+z_0)}{u^*} \frac{\partial \mathcal{V}}{\partial z}, \qquad (6.4)$$

where z_0 is the roughness length ($z_0 = 0.10$ m) and $\mathcal{V}$ the amplitude of the horizontal velocity vector.

A comparison of the results of Experiment II with the observational results of Businger *et al.* (1971) provides a severe test of the model's ability to simulate the statistical behavior of the surface boundary layer. Fig. 21 shows this comparison for ϕ_m and ϕ_H as a function of z/L_m. The dashed curves in this figure represent the observational data, while the points show numerical results from Experiment II averaged over 1 hr for different times of the day and for different levels such that $|z/L_m| \leqslant 3$. The general behavior of the observational ϕ_H is reproduced by the model with large nighttime values and low daytime values. The numerical data are slightly lower than the observational results at night[2] and slightly higher during the day. Agreement of

---

[2] We must point out, however, that some observations from the source of Businger's data are inside of our scattered data for large values of z/L_m [~ 3].

numerical values of ϕ_m with observed values is less satisfactory, particularly for unstable daytime conditions in which model values are typically several times larger than observed values. This discrepancy can be attributed to the fact that the x component of the surface stresses ($z \leqslant 10$ m) was improperly simulated due to the imposed lower boundary condition on vorticity, as was mentioned earlier with regard to Fig. 17. We hope to overcome this difficulty by using a more complete formulation of the surface boundary layer in the three-dimensional primitive equation model which we are presently developing.

7. Summary and conclusions

In this paper we have presented and used a two-dimensional mesoscale atmospheric model to study unsteady dynamic processes which occur in the planetary boundary layer and above. The model reproduces turbulent fluxes of heat and momentum both by the explicit modeling of resolvable turbulent eddies and by a single parameterization, at all levels of the model, of vertical fluxes due to subgrid-scale eddies. The unsteady behavior of horizontally-averaged profiles of temperature and velocity respond realistically to a diurnally-varying heating of the atmosphere at the surface. In particular, the time variation of lapse rates and the times of occurrence of maximum and minimum

temperatures at various levels in the lower boundary layer are predicted quite well by the model.

Presentation of the horizontal as well as the vertical variation of the predicted atmospheric quantities shows large eddy activity in the solution during the daytime. These eddies represent the primary means by which heat and momentum are transferred vertically within the boundary layer above the first 10 m of the model during the day. A remnant of this daytime mixing persists into the night in the upper levels of the PBL, but the strength of this eddy activity gradually decreases with time after sunset. A two-dimensional contour plot of the deviation of potential temperature from its horizontally-averaged mean values shows the development of a shallow heat island after midnight above the surface heat source which was generated by our use of a Gaussian spatial distribution for the assumed heat flux at the ground.

The model reproduces the behavior of atmospheric heat fluxes within the PBL with the distribution of heat fluxes and the height of the penetrative convection layer behaving realistically. The diurnal behavior of heat flux shows that boundary layer activity is confined to the lower 200 m of the atmosphere at night while extending up to 800 m during the daytime. Total eddy diffusivity (including transport due to resolved eddies) reached peak values of $\sim$100 m^2 sec^{-1} within the planetary boundary layer during the day compared to maximum parameterized subgrid-scale values of less than 1 m^2 sec^{-1}.

With regard to the velocity field, strong inertial oscillations occur in a so-called Ekman layer in the model. The behavior of the vertical transfer of momentum is generally satisfactory although low values of shear in the x velocity near the ground cause the predicted shear stress to be too low in the first few meters above the surface. This improper behavior of u is largely due to the necessary use of a vorticity boundary condition to constrain the x-velocity u at the surface in the current model. This inadequacy of the present formulation will be corrected by the use of primitive equations in the three-dimensional model which is under development at GFDL. Further improvement in the behavior of the surface boundary layer is expected in this new model through the use of a heat balance calculation for the soil-atmosphere interface and the use of a special treatment of the surface boundary layer which takes account of the local variation of turbulent kinetic energy in the calculation of the local eddy diffusivity.

REFERENCES

Arakawa, A., 1966: Computational design for long-term numerical integration of the equations of motion: Two-dimensional incompressible flow, Part I. *J. Comput. Phys.*, **1**, 119–143.

Businger, J. A., J. C. Wygaard, Y. Izumi and E. F. Bradley, 1971: Flux-profile relationships in the atmospheric surface layer. *J. Atmos. Sci.*, **28**, 181–189.

Clarke, J. H., 1969: Nocturnal boundary layer over Cincinnati, Ohio. *Mon. Wea. Rev.*, **97**, 582–589.

Clarke, R. H., A. J. Dyer, R. R. Brooks, D. G. Reid and A. J. Troup, 1971: The Wangara experiment: Boundary layer data. Tech. Paper 19, Div. Meteor. Phys., CSIRO, Melbourne, Australia.

Deardorff, J. W., 1969: Numerical study of heat transport by internal gravity waves above a growing unstable layer. *Phys. Fluids*, Suppl. II, **12**, II-184 to II-194.

Estoque, M. A. 1963: A numerical model of the atmospheric boundary layer. *J. Geophys. Res.*, **68**, 1103–1113.

Globe, S., and D. Dropkin, 1959: Natural convection heat transfer in liquids confined by two horizontal plates and heated from below. *J. Heat. Trans.*, **81**, 156–185.

Hess, G. D., and R. H. Clarke, 1973: Time spectra and cross-spectra of kinetic energy in the planetary boundary layer. *Quart. J. Roy. Meteor. Soc.*, **99**, 130–153.

Ingersoll, A. P., 1966: Thermal convection with shear at high Rayleigh number. *J. Fluid Mech.*, **25**, 209–228.

Kraichnan, R. H. 1962: Turbulent thermal convection at arbitrary Prandtl number. *Phys. Fluids*, **5**, 1374–1389.

Lettau, H., and B. Davidson, 1957: *Exploring the Atmosphere's First Mile*, Vol. 2. New York, Pergamon Press, 202 pp.

Lilly, D. K., 1962: On the numerical simulation of buoyant convection. *Tellus*, **14**, 148–172.

——, 1965: On the computational stability of numerical solutions of time dependent non-linear geophysical fluid dynamics problems. *Mon. Wea. Rev.*, **93**, 11–26.

——, 1972: Wave momentum flux—a GARP problem. *Bull. Amer. Meteor. Soc.*, **53**, 17–23.

Lumley, J. L., and H. A. Panofsky, 1964: *The Structure of Atmospheric Turbulence*. New York, Interscience, 239 pp.

Lykosov, V. N., 1972: Unsteady state in the planetary boundary layer of the atmosphere. *Izv. Atmos. Oceanic Phys.*, **8**, 85–91.

McElroy, J. L., 1972: A numerical model of the nocturnal urban boundary layer. *Proc. Symp. Air Pollution, Turbulence, and Diffusion*, H. W. Church and R. E. Luna, Eds., Sandia Corp., Albuquerque, N.M.

Ogura, Y., and N. A. Phillips, 1962: Scale analysis of deep and shallow convection in the atmosphere. *J. Atmos. Sci.*, **19**, 173–179.

Orlanski, I., 1973: Trapeze instability as a source of internal gravity waves, Part I. *J. Atmos. Sci.*, **30**, 1007–1016.

——, and B. B. Ross, 1973: Numerical simulation of the generation and breaking of internal gravity waves. *J. Geophys. Res.*, **78**, 8808–8826.

Pandolfo, J. P., 1971: Numerical experiments with alternative boundary layer formulations using BOMEX data. *Boundary Layer Meteor.*, **1**, 277–289.

Priestley, C. H. B., 1954: Convection from a horizontal surface. *Aust. J. Phys.*, **7**, 176–201.